FINAL REPORT

Regional Probabilistic Liquefaction Hazard Mapping for the Sacramento – San Joaquin River Delta

Prepared by:

Greenfield Geotechnical LLC
March 30, 2022

GREENFIELD
GEOTECHNICAL
Advanced geotechnical and earthquake engineering solutions

PROJECT INFORMATION SUMMARY

USGS Award Number:	G21AP10019-00
Project Title:	Regional probabilistic liquefaction hazard mapping for the Sacramento – San Joaquin Delta: Collaborative Research with Greenfield Geotechnical and the United States Geological Survey
Principal Investigator:	Dr. Michael Greenfield, P.E., Ph.D. (PI) Greenfield Geotechnical LLC 5733 SE 70th Ave Portland, OR 97206 540.392.1741 / mike@greenfieldgeotechnical.com
Term Covered By Award:	January 1, 2021, through December 31, 2021

Plain language summary

When saturated, loose, sandy soil is shaken by an earthquake, the soil can temporarily behave like a fluid in a process called liquefaction. You can experience soil liquefaction by wiggling your feet in sand underwater at the beach until your feet sink. Liquefied soils are very soft, flow easily, and can't support structures like buildings or levees. For soils to liquefy, they need to be saturated and sandy and the earthquake ground shaking needs to be sufficiently strong. If the layer of liquefied soil is thick enough, liquefaction can cause damage to the ground surface including ground cracking, sand boils, settlement, or building foundation strength loss.

Many of the lands surrounding the Sacramento and San-Joaquin River Delta are composed of wet, loose, sandy soil that could liquefy during a large earthquake. Past earthquakes have damaged levees on Bacon Island, Venice Island, and Empire Tract, even though the earthquakes were very far away and caused only modest ground shaking. While the historical damage to levees appears to have been caused by a different mechanism (peat foundation instability), the potential for liquefaction in the Delta presents a serious hazard. A large earthquake originating in the San Francisco Bay area or within the Delta could cause significant liquefaction that may result in much greater damage than historic earthquakes.

Engineers usually find liquefiable soils by drilling borings or pushing probes into the ground. But, over a large area like the Delta, engineers can't drill enough borings to fully understand the groundwater and soil conditions for liquefaction analyses. With help from the USGS, Greenfield Geotechnical has created a new technique that enables engineers to better understand the subsurface conditions that could lead to liquefaction, even where local borehole data is not widely available. We collected information from over 2,700 wells, borings, and probes to build a model of the subsurface groundwater, geology, and soil conditions. Our model allows us to use the same methods that engineers use to design large buildings with many closely spaced borings but includes additional steps to account for the inherent uncertainty between widely-spaced borings. We used our model in a supercomputer to understand where liquefaction is most likely during a very large earthquake on the Hayward Fault near Oakland. The model shows that liquefaction could damage roadways throughout the Delta as well as the levees protecting the lands around the Contra Costa Canal.

We also simulated the damage from a possible earthquake within the Delta. This earthquake would be much closer than the Hayward Fault earthquake and ground shaking would be much stronger. The model shows that liquefaction could be widespread during a fault rupture within the Delta. Many of the levees protecting the islands in the Delta are likely to be damaged. Liquefaction could extend far inland and affect the communities of Oakley and Sand Hill.

Large plates of the areas of ground damage from these two scenarios are available at the back of this report. These plates and other information in this report may be helpful to understand the locations where roadways, levees, pipes, power lines are most likely to be damaged by liquefaction from seismic activity in the region.

Table of Contents

Abstract

The Sacramento and San Joaquin River Delta (herein 'the Delta') is home to important ecological, agricultural, and water resources for the State of California. Lands within the Delta are protected by a series of levees founded on variable and complex layers of sands, silts, clays, and organic peat deposits. Many of the sandy soils supporting the levees are loose and liquefiable such that even modest ground shaking from an earthquake could trigger liquefaction, potentially resulting in ground damage and impacts to critical lifeline infrastructure including roadways, levees, pipelines, electrical transmission facilities, and underground water conveyance facilities. Existing liquefaction hazard maps in the Delta, and throughout the nation, are based primarily on correlations with ground surface geology and topography. Such maps identify geologic units that could contain liquefiable soils but do not necessarily reflect known subsurface conditions that influence liquefaction. Site-specific geotechnical investigations often show that the extent and magnitude of liquefaction damage depend on hydraulic conditions, the soil's susceptibility to liquefaction, fine-grained particle content, cyclic resistance, and the depth and connectivity of liquefiable soil layers. While these properties are typically measured through extensive geotechnical subsurface investigations, we have collected data from over 2,700 borings, wells, and cone penetration probes to facilitate a probabilistic geospatial liquefaction hazard analysis within the Delta.

This project seeks to address the spatial variability of liquefiable soil deposits by developing 3D Gaussian process (GP) models of groundwater depth, geologic deposit classification, soil behavior classification, and penetration resistance. The GP models quantify the uncertainty in-between investigation locations and also converge to the measurement uncertainty at boring and probe locations. We utilize a probabilistic extension of the site-specific geotechnical liquefaction triggering methods developed by USGS staff and Greenfield Geotechnical with the GP models to calculate the probability of liquefaction triggering at any 3D point within the project domain. We then use the GP models to calculate the probability of a thick enough layer of soil liquefying to produce ground damage, effectively unifying site-specific and deposit-scale liquefaction analyses.

We have selected an approximately 750 km^2 pilot study area in the Delta for a pilot study. Using the independent GP models for groundwater depth, geologic deposit classification, soil behavior classification, and penetration resistance, we evaluate M_w 7.1 Hayward Fault and M_w 7.3 Midland Fault Zone earthquake scenarios and provide maps of the probability of liquefaction ground damage within the pilot study area. The results from these two scenarios show that critical infrastructure lifelines could be damaged during an earthquake originating outside of the Delta and extensive damage is likely from an earthquake originating inside of the Delta.

1. Introduction

1.1. Background

The Sacramento – San Joaquin River Delta (see Figure 1.1) is part of a complex river system that supplies fresh water to more than two-thirds of California's population. The municipal and agricultural demands for water are so high that only about half of the water in the Delta ever reaches the ocean. The Delta is also home to a rare estuarine ecosystem of more than 500 plant, fish, and bird species. The balance of ecological, municipal, and agricultural water use in the Delta is complex and nuanced, but the water conveyance system, the human population, and the natural ecosystem could all be severely impacted by liquefaction during an earthquake.

The water conveyance system through the Delta consists of a complicated network of levees, bays, and channels that transports freshwater from the foothills of the Sierra Nevada Mountains to southern California. The levees along the river channels help protect the over 500,000 human inhabitants from flooding, while also maintaining water quality and protecting native brackish marshlands from freshwater inundation. Despite the critical roles of the levees and water conveyance systems, recent studies[1,2] have found that the levees are vulnerable to soil liquefaction and damage during an earthquake. Levee failures could be devastating to the state's economy and would damage the fragile natural ecosystem. Alternative concepts to create new water conveyance systems would likely cost more than $10 billion[3].

Other elements of critical infrastructure in the Delta, such as roadways, electrical transmission, and buried utilities are also vulnerable to liquefaction. Recent seismic hazard studies within the Delta have primarily focused on the levees and neglected the other elements of critical infrastructure. Liquefaction of the artificial embankment fills and natural sandy soil deposits could destroy roadways, block emergency access, and damage electrical, gas, and water transmission facilities. Comprehensive liquefaction hazard and resiliency analyses should not only consider the levees but should also consider liquefaction hazards within the interior of the islands, at the depths of possible buried infrastructure, and in population centers.

Several seismic sources in the area could produce strong enough ground shaking to liquefy saturated artificial fills and natural soils. The consequences of liquefaction could include ground settlement, foundation failure, ground cracks, sand boils, and ground deformations caused by lateral spreading. With such high stakes, it is important to completely understand the liquefaction hazards in the Delta.

[1] California Department of Water Resources (2008). Delta Risk Management Strategy (DRMS).
[2] Delta Stewardship Council (2017). Delta Levees Investment Strategy. Final Report. ("DLIS").
[3] California Department of Water Resources (2015). Delta Habitat Conservations & Conveyance Program.

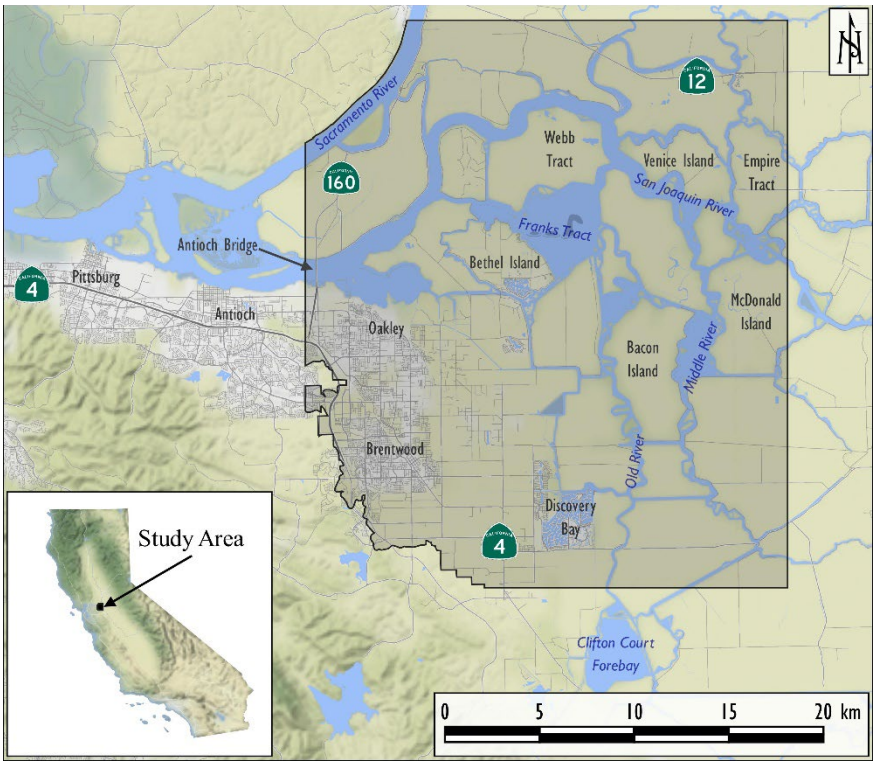

Figure 1.1 – Pilot Study Area and Vicinity Map

1.2. The conventional approach to liquefaction hazards

Liquefaction occurs when saturated granular soils are subjected to cyclic loading, which distorts the soil structure and causes loosely packed groups of particles to collapse, increasing porewater pressure in the soil mass. As pore pressure increases, the soil begins to lose strength and may even temporarily behave as a viscous fluid in the most extreme cases. Liquefaction can result in settlement of the ground surface, large lateral deformations, decreased bearing capacity, settlement of shallow foundations, and reduced axial and lateral capacities of pile foundations.

Liquefaction only occurs in saturated soils, and as such the depth to groundwater is an important component of liquefaction hazard analyses. Shallow groundwater also increases the hydrostatic pore pressure in the soil and reduces the effective stress, which can increase the intensity measure associated with dynamic loading from an earthquake (cyclic stress ratio). The depth at which the soil is saturated and nonzero pore pressures can develop is defined as the phreatic surface. Soils below the phreatic surface are saturated, can develop excess pore pressure during shaking, and can liquefy if they exhibit sand-like behavior and the cyclic stresses from the earthquake exceed the cyclic resistance of the soil.

Geotechnical engineers usually characterize liquefaction hazards through a series of borings or probes spaced less than about 100 m apart. Such site-specific liquefaction analyses often show that thick, shallow deposits of saturated, loose, fine sand with little silt or clay are more likely

to produce ground damage than thin, deep deposits of dense, well-graded silty sand. Unfortunately, subsurface conditions cannot be investigated at a site-specific level of detail for infrastructure that is distributed over many kilometers, like the Delta levee system.

However, site-specific analyses for consequences of liquefaction may be extended to deposit-scale analyses by considering the groundwater table, the soil's plasticity index, geology, and penetration resistance as uncertain, random variables. These subsurface properties are rarely well-defined for a whole region, or sometimes even for a specific project, but sufficient data may be available to characterize the trends and uncertainties of these properties for geologic deposits that are well-known to contain liquefiable soils.

1.3. Motivation for an improved regional liquefaction methodology

Existing liquefaction hazard maps in the Delta, and throughout the nation, are based primarily on correlations with ground surface geology and topography[4]. Such maps typically show which geologic units could contain liquefiable soils, but do not necessarily reflect localized topographic, hydraulic, and soil conditions that are known to influence liquefaction. Past regional liquefaction hazard projects in the Delta have recognized the need to extend site-specific geotechnical analyses to a regional scale. Real and Knudsen[5] accomplished this by incorporating data from over 3,000 borehole penetration tests to develop profiles of average geotechnical properties for various geologic deposits. While their work represents an important milestone in understanding liquefaction hazards at a regional scale, the geologic deposit averages still include a great amount of uncertainty in the local soil and groundwater conditions that are associated with liquefaction. Other past studies utilizing geologic deposit averages (e.g., Greenfield and others[6]) have identified that the geologic deposit averages may overpredict the footprint of liquefaction and underpredict the magnitude of ground damage at high hazard locations.

While certain geologic units are known to contain soils that are susceptible to liquefaction, the probability of liquefaction-induced ground damage depends on the intensity of localized ground shaking, groundwater depth, and soil conditions. These factors can vary widely within a geologic deposit. However, the performance of infrastructure lifelines during an earthquake, including levees, pipelines, roadways, and electrical transmission facilities, depends on the potential for ground damage at specific locations; hence the geologic unit-based averages may not

[4] E.g., Youd, T.L., Tinsley, J.C., Perkins, D.M., King, E.J., & Preston, R. (1978). Liquefaction Potential Map of San Fernando Valley, California. In *Int. Conf. on Microzonation for Safer Construction, 2nd, San Francisco* (Vol. 1, pp. 267-278); Holzer, T.L., Noce, T.E., & Bennett, M.J. (2011). Liquefaction probability curves for surficial geologic deposits. *Environmental and Engineering Geoscience*, 17(1), 1-21.

[5] Real, C.R., Knudsen, K.L., and Woods, M.O. (2010). "Application of New Liquefaction Hazard Mapping Techniques to the Sacramento-San Joaquin Delta." *AGU Fall Meeting Abstracts*. ("Real and Knudsen (2010)").

[6] Greenfield, M., Nisar, A., Hitchcock, C., McCormick, E., and Nelson, R. (2018). Regional-scale liquefaction hazard mapping using subsurface data. 11th U.S. National Conference on Earthquake Engineering, Los Angeles, June 25, 2018.

provide sufficiently localized information to evaluate possible breaks in the networks.

More detailed, quantifiable estimates of the soil and groundwater conditions associated with liquefaction hazards are necessary for seismic resilience planning at the regional scale. Localized knowledge of which areas are likely to be most susceptible to damage can help decision-makers prioritize long-term plans for mitigation efforts and first responders know which areas are more likely to be damaged. Likewise, the uncertainty in subsurface conditions at poorly sampled locations should be quantified and understood to help identify and prioritize locations for additional subsurface investigations.

1.4. Project objectives

The overall goal of the project is to demonstrate that the concepts embedded in site-specific liquefaction methods may be extended to evaluate the liquefaction hazard at a regional scale through geospatial statistics. The project utilizes geostatistical models previously developed by Greenfield and Grant[7] to predict the probability of liquefaction ground damage on a closely spaced 3D grid throughout the pilot study area. The geospatial models are trained using maximum likelihood estimation with available subsurface data, such that they approximate the measurement uncertainty associated with site-specific investigations at locations where sufficient subsurface data is available. Conversely, at locations where limited data are available, the model approaches the deposit-scale average values, effectively unifying site-specific geotechnical methods near borehole locations with the regional composite-average method developed by Real and Knudsen.

The second objective of this project is to provide liquefaction hazard estimates within the Delta to support the USGS's *Improved understanding of active faults and liquefaction potential in the Sacramento – San Joaquin Delta* project. The models developed for this study have been created in collaboration with the USGS and a panel of experts, who have provided comments based on a series of panel discussion sessions. While the project is a pilot study, the results may be directly applicable for decision-makers to help understand the potential for liquefaction hazards in the Delta.

2. Geology and Seismic setting of the Sacramento and San Joaquin Delta

2.1. Topography

The Sacramento-San Joaquin Delta is part low-lying inland estuary of the San Francisco Bay and part man-made reclamation project. Before human intervention, tidal marshes and channels intertwined with natural levees and sand dunes to form a complex, but resilient, tidal freshwater ecosystem. The Delta of today is composed of a series of low-lying tracts and islands protected by man-made levees constructed on top of the natural levees. Many of the islands have now sunk below sea level as reclamation and agriculture have pumped water from the former

[7] Greenfield, M.W. and Grant, A. (2020). "Probabilistic regional-scale liquefaction triggering modeling using 3D Gaussian processes." *Soil Dynamics and Earthquake Engineering*, 134.

marshes[8]. A series of canals and aqueducts also transport water through the Delta to other parts of California. The resulting topography of the pilot study area is largely characterized by low-lying hills and gently graded suburban areas to the west; levees, aqueducts, canals, and rivers to the north; and low-lying islands, levees, and channels to the east and south.

Ground surface digital elevation models (DEM) are available from the California Department of Water Resources (DWR) based on 2017 Lidar data[9]. Products include a high-resolution 0.5 m Lidar-based DEM that covers much of the Delta. We have downloaded and processed the Lidar-derived DEM, converted the DEM elevation from ft to m, and then down-sampled the DEM to 3 m for our analyses. All USGS 3D Elevation program DEMs and the DWR Lidar DEM are referenced to the datum of NAVD88 with elevation in m. Some older boring logs collected for this study are referenced to NGVD29, and we used spatial conversion information provided by Real and Knudsen[10] to convert elevations in NGVD29 to NAVD88 for this project.

Bathymetry data is also available within some of the rivers but does not extend throughout the study area. The data indicate channels of the San Joaquin River may extend as deep as elevation -18 m. The majority of bathymetry used in the study comes from 2 m DEMs[11] developed by USGS and DWR and referenced to NAVD88(m). Bathymetric data covering additional portions of the study area was sourced from DWR's Delta Bathymetry Catalog[12]. Where necessary, bathymetry elevations were converted to m from ft. Where bathymetry was unavailable, we approximated the channel elevation based on nearby channels with available bathymetric data.

Throughout the Delta, the levees vary considerably in both height and composition[13]. We reviewed the Lidar data to determine the height of a given levee as the difference between the crown elevation and the approximate elevation of the subsided interior of the island. We use the levee height to approximate the fundamental period of vibration of the levee.

2.2. Geologic deposits

Atwater[14] provides comprehensive, detailed maps of the surficial geology of the Delta along with geologic contact elevations at many pre-1982 borehole locations. Additional work by

[8] Ingebritsen, S.E. and Ikehara, M.E. (1999). Sacramento-San Joaquin Delta: the sinking heart of the state. Land Subsidence in the United States. Circular, 1182, pp.83-94.
[9] http://gisarchive.cnra.ca.gov/iso/ImageryBaseMapsLandCover/LIDAR/DeltaLIDAR2017
[10] Real and Knudsen (2010). See note 5.
[11] https://data.cnra.ca.gov/dataset/san-francisco-bay-and-sacramento-san-joaquin-delta-dem-for-modeling-version-4-2
[12] https://gis.water.ca.gov/app/bathymetry/
[13] California Department of Water Resources (2008). Delta Risk Management Strategy (DRMS), Phase 1, Topical Area: Levee Vulnerability, Final. URS Corporation/Jack R. Benjamin & Associates, Inc.
[14] Atwater, B.F. (1982). Geologic Maps of the Sacramento – San Joaquin Delta, California, MF-1401.

Knudsen and others[15] and Witter and others[16] have produced comprehensive GIS-based geology maps within the study area. We have grouped members of the geologic deposits mapped by Atwater based on their known liquefaction susceptibility characteristics and the density of available data. The resulting geology classifications are fill (Af), Holocene alluvium (Qha), Holocene delta peat (Qhm), late Pleistocene dunes (Qd), and undifferentiated middle Pleistocene and older deposits (Qp). An additional deposit has been added for Holocene alluvium of historical channels (Qhc) based on data from Hitchcock[17]. Table 2.1 lists the units described by Atwater that have been grouped into the broader classifications for this study. Figure 2.1 shows the ground surface geology with the six deposits throughout the study area. While we acknowledge that some of these classifications may be somewhat broad and could be subdivided into more units, the spatial variability within each deposit is considered in subsequent analyses.

Table 2.1: Geologic deposit designation for liquefaction analyses within the study area

Geologic deposit	Abbreviation	Atwater designation
Fill	Af	Af
Holocene alluvium	Qha	Qfp, Qymc,
Holocene channel deposits	Qhc	late Holocene waterways
Holocene delta peat	Qhm	Qpm
late Pleistocene dunes	Qd	Qm2e
undifferentiated middle Pleistocene & older soils	Qp	Qom, Qm, Qomc

[15] Knudsen, K.L., Sowers, J.M., Witter, R.C., Wentworth, C.M., Helley, E.J (2000). Preliminary maps of the Quaternary deposits and liquefaction susceptibility, nine-county San Francisco Bay Region, California: A digital database: U.S., Geological Survey Open-File Report 00-444.

[16] Witter, R.C., Knudsen, K.L., Sowers, J.M., Wentworth, C.M., Koehler, R.D. and Randolph, C.E. (2006). Maps of Quaternary deposits and liquefaction susceptibility in the central San Francisco Bay region, California: U.S. Geological Survey Open-File Report 2006-1037: https://pubs.usgs.gov/of/2006/1037/.

[17] Hitchcock (2021). Personal communication.

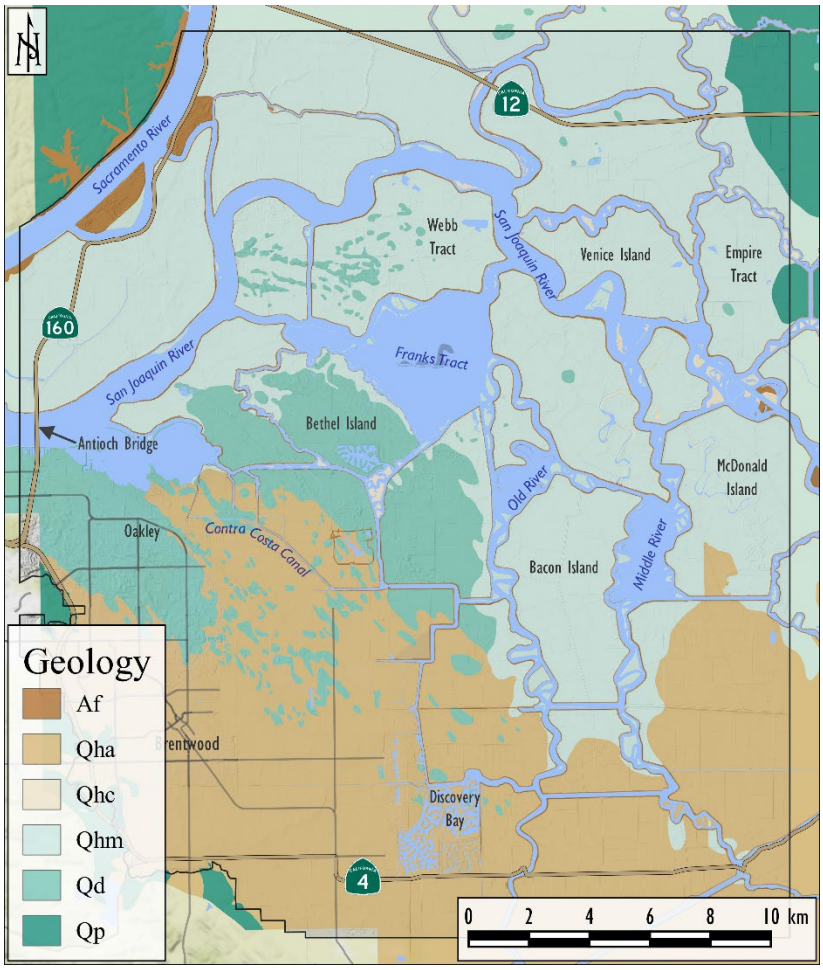

Figure 2.1 – Geology Map

2.3. Seismic setting

Potential seismic hazards that could influence liquefaction hazards within the Delta include highly active faults near the San Francisco Bay area that are associated with the San Andreas Fault system, as well as potentially active but concealed faults within the Delta, such as the Midland Fault Zone. The faults near the San Francisco Bay, including the Calaveras, Hayward-Rodgers Creek, and San Andreas Faults, are generally well-constrained by surface ruptures and are known to be highly active, but lie more than 25 km from the study area. Earthquakes on these faults likely occur relatively frequently, but the rupture distance attenuates much of the shaking intensity. Conversely, faults within the Delta are concealed without historical evidence of surface rupture, leading to considerable uncertainty in the faults' activity, size, and location. The DRMS report provides a detailed summary of potential seismic sources that could impact the Delta based on the

available information at the time of the report. Other, USGS-funded studies[18] have also investigated seismicity in the Delta based on geomorphology, well logs, and seismic reflection data. A USGS-led study titled *Improved understanding of active faults and liquefaction potential in the Sacramento – San Joaquin Delta* is currently underway to further investigate seismic activity within the Delta.

2.4. Historic earthquake damage

Historical ground shaking within the Delta is largely limited to distant earthquakes, including the 1980 M5.9 Livermore earthquake and the 1984 M6.2 Morgan Hill earthquake. Finch[19] reports damage to levees on Bacon Island and Empire Tract following the Livermore earthquake and Venice Island and Webb Tract during the Morgan Hill earthquake. Figure 2.2 shows a photograph of the levee damage on Bacon Island following the Livermore earthquake. Figure 2.3 provides a map of the peak ground acceleration from these events with the locations and descriptions of observed levee damage.

[18] Unruh, J.R., Hitchcock, C.S., Hector, S. and Blake, K. (2009). Characterization of Potential Seismic Sources in the Sacramento-San Joaquin Delta, California: Final Technical Report, U.S. Geological Survey, National Earthquake Hazards Reduction Program, Award Number 08HQGR0055, 45 p.

[19] Finch, M. (1985). "Earthquake Damage in the Sacramento – San Joaquin Delta, Sacramento and San Joaquin Counties" *California Geology* 38(2): 39-44.

Figure 2.2 – Photograph of levee damage on Bacon Island. Finch (1985) reports "A 250-foot land-side rotational slip-out dropped several feet during the Livermore earthquake of January 24, 1980.

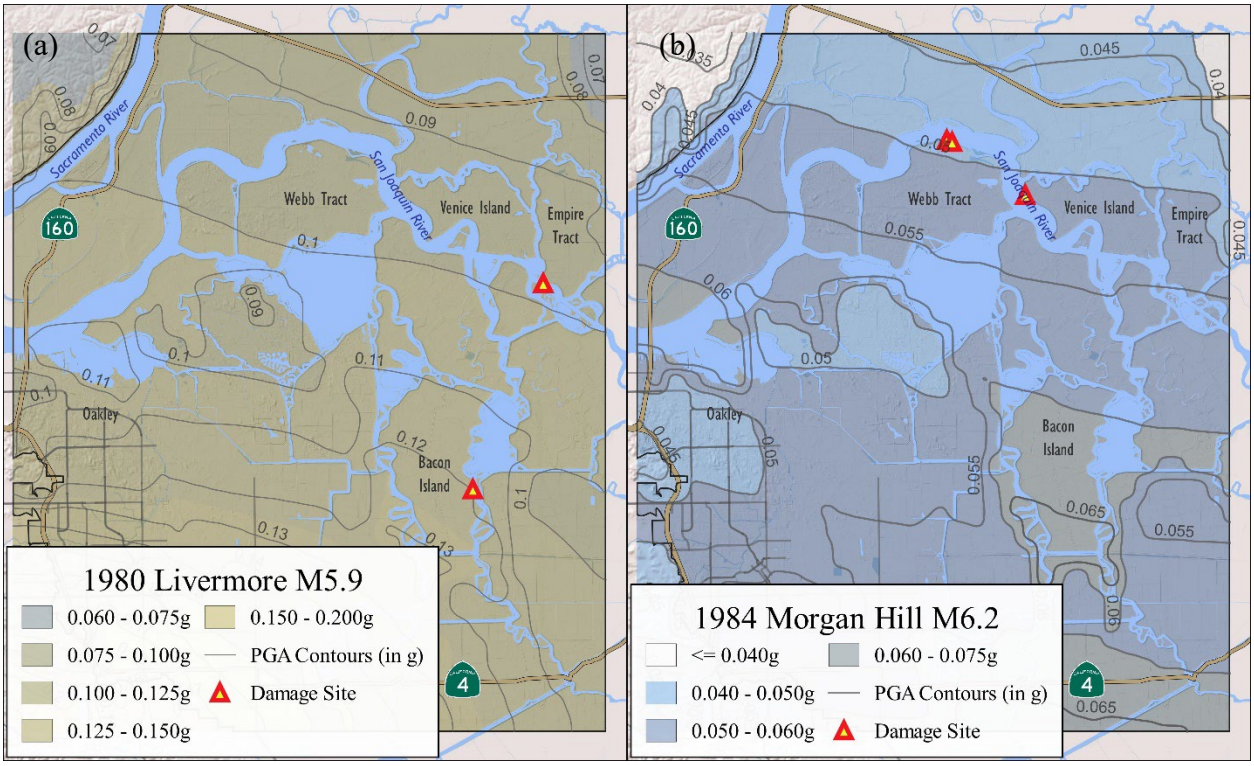

Levee Damage from 1980 Livermore M5.9	*Levee Damage from 1984 Morgan Hill M6.2*
Bacon Island: A 250-foot land-side rotational slip-out dropped several feet. This damage was cited by the 1980 DWR Delta seismicity hazards report as possible earthquake related damage.	Venice Island: A pre-existing 25-foot-long crack lengthened 75 feet and the land side of levee dropped 2 inches. This site was inspected by the island caretaker and DWR employees before and after the earthquake.
Empire Tract: A 200-foot land-side rotational slip-out dropped 6 inches. It was reported by a local resident and a DWR employee.	Webb Tract: Six parallel cracks one inch wide and 75 feet long were noticed minutes after the earthquake. They were not present the day before the earthquake.
	Webb Tract: A 25-foot long crack one inch wide was noticed at the same time.

Figure 2.3 – Historical levee damage reported by Finch (1985) during (a) M5.9 Livermore earthquake and (b) M6.2 Morgan Hill earthquake

The estimated peak ground acceleration values during either event were relatively modest, illustrating the fragile nature of the levees in the Delta. The failure modes associated with ground damage from these historic events are difficult to interpret based on the descriptions and could be associated with liquefaction or foundation instability of levees founded on peat or soft clay soils.

2.5. Seismic hazards

Broadly, the uncertainties in seismic sources within the Delta are most appropriately evaluated using probabilistic seismic hazard assessment (PSHA). The DRMS study provides time-dependent hazard curves based on the information available at the time of the study. The report indicates the highly active faults within the San Francisco Bay area, particularly the Hayward Fault, are the greatest contributor to the hazard at very short return periods (about 10 years). Conversely, the Midland Fault Zone is by far the greatest contributor to the hazard at return periods of interest to engineered structures (about 1,000 years).

The focus of this project is to evaluate the uncertainty in subsurface conditions at a regional scale that could influence liquefaction hazards. The simplified liquefaction triggering method that serves as the basis of the regional scale approximations is developed for deterministic scenarios, with earthquake magnitude and peak ground acceleration considered as scalar input values. While future studies should incorporate the uncertainties associated both with the uncertainty in subsurface conditions and the varied range of seismic sources, we have selected an M_w 7.1 Hayward Fault rupture scenario originating near Oakland[20] and an M_w 7.3 Great Valley Midland Fault Zone rupture[21] for this study. Figure 2.4 shows the peak ground acceleration within the study area associated with each scenario.

[20] Detweiler, S.T. and Wein, A.M. (2018). The HayWired Earthquake Scenario-Earthquake Hazards. Scientific Investigations Report 2017-5013-A-H. USGS.

[21] Building Seismic Safety Council (BSSC) (2015). NEHRP Recommended Seismic Provisions for New Buildings and Other Structures, Volume 1: Part 1 Provisions, Part 2 Commentary, FEMA P-1050-1, Washington, D.C., 555 pp.

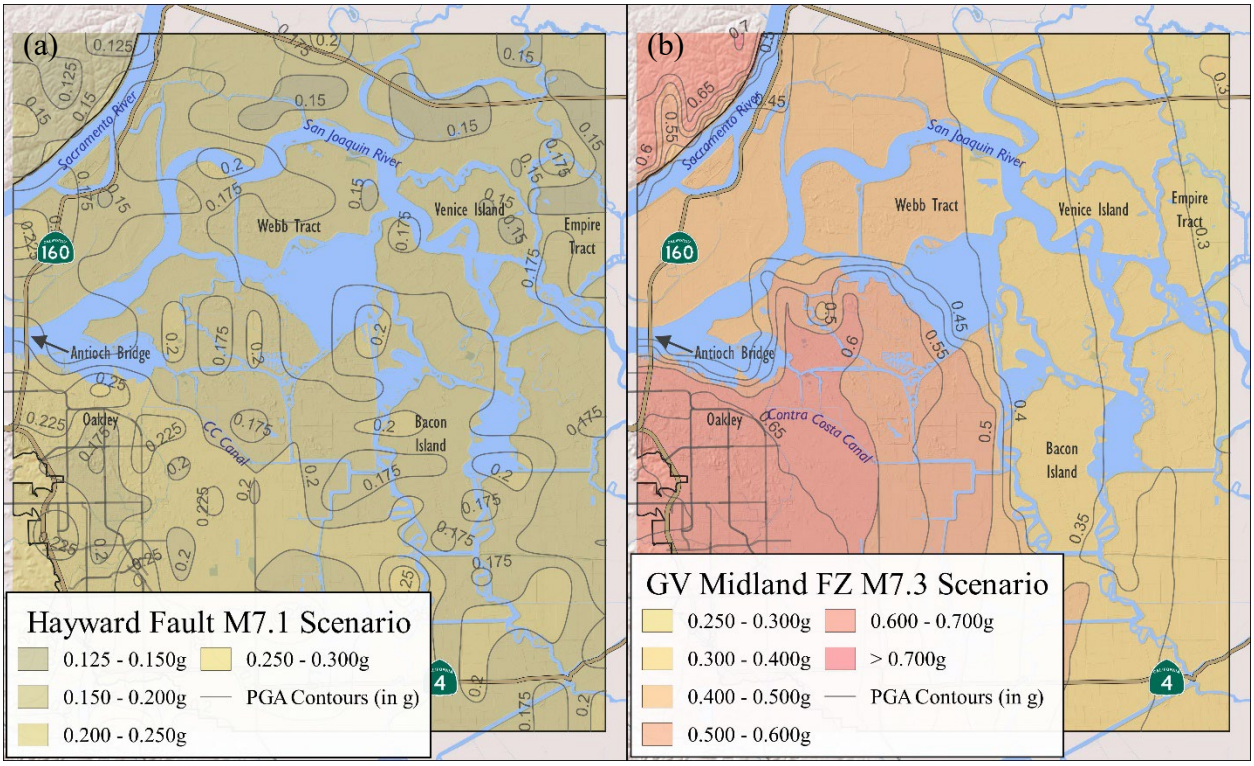

Figure 2.4 – Earthquake scenarios selected for analysis (a) M7.1 Hayward Fault earthquake and (b) M7.3 Great Valley Midland Fault Zone earthquake

3. Subsurface data

3.1. Wells

DWR's online portal[22] provides a comprehensive database of well completion reports within the study area. Data from many of these reports include either the depth that water was first encountered (wells installed with augers) or the depth of static water in monitoring wells. A subset of the reports includes wells that are screened within 10 m of the static groundwater elevation with an approximate measurement of the phreatic groundwater elevation. The water surface elevation reported by DWR is relative to the NAVD88 datum in feet, which we convert into elevation in meters. The DWR portal also provides a georeferenced shapefile with approximate well locations. The scanned well completion form associated with each well provides a more accurate location, and we have reviewed and updated the georeferenced shapefile accordingly. Data from 370 well completion reports with static water elevations observed between September 1962 and September 2020 are available within the project area.

[22] California Department of Water Resources, Well Completion Reports: https://data.ca.gov/dataset/well-completion-reports (October 2021).

DWR's online portal[23] also provides monitoring well time-series data. We select wells from the monitoring well dataset that are described as observation wells that are less than 50 m deep. Data from 56 monitoring wells, observed between August 1998 to October 2020, are available within the study area. The selected monitoring well database includes over 4,581 observations, with up to 290 observations per well.

California Geologic Survey (CGS) provides a comprehensive georeferenced dataset of boring logs[24], many of which were drilled using methods that allow for the observation of groundwater during drilling. Data from 464 borings, drilled between July 1964 and June 2015, include groundwater observations at the time of drilling.

3.2. Lithology logs

Atwater[25] provides a map of the thickness of peat deposits and the contact elevations of basal deposits based on hundreds of early (pre-1982) subsurface investigations. The maps only indicate the elevation of the deeper, stiffer material and do not explicitly classify the deeper geologic deposits. We have interpreted the geologic deposit classification based on the proximity of the boring to nearby geologic outcrops and more recent borings with geologic descriptions. The contact elevation of each deposit is listed in feet NGVD29, which we have converted to elevation in meters NGVD88. Atwater's maps do not explicitly note the thickness of levee fill, which may have been modified since the pre-1982 investigations. We have added additional fill thickness to the layers based on the current levee elevation based on the Lidar-derived 3 m DEM.

The Atwater lithology maps include 654 borings within the study area. We convert the geologic contact elevations from the maps into lithology pseudo-samples at 1.5 m intervals for a total of 4,676 samples within the study area.

3.3. Boring logs

CGS[26] provides a digital borehole database from 805 boring logs within the study area. Each boring includes multiple SPT samples with records of the date of sample collection, drilling and sampling methods, a description of the sample, and penetration test data. Laboratory test data is also associated with many of the SPT samples, including Atterberg limits testing, soil unit weight, moisture content, grain size analysis, and fines content data. Soil behavior classifications and fines content estimates are needed for liquefaction susceptibility and triggering analyses. In the absence of laboratory data, we assign fines content and soil behavior classifications to samples based on the samples' description and the laboratory test data from nearby samples as discussed

[23] California Department of Water Resources, California Statewide Groundwater Elevation Monitoring (CASGEM) Program: https://water.ca.gov/programs/groundwater-management/groundwater-elevation-monitoring--casgem (October 2021)
[24] Frost, E. (2021). Personal communication.
[25] Atwater (1982). See note 14.
[26] Frost (2021). See note 24.

in Section 3.5. We also associate each sample to a specific geologic deposit based on the samples' description, plasticity information, and location in conjunction with the available geologic maps. The dataset contains 4,427 samples from 805 borings drilled between July 1964 and April 2016.

DWR and the USGS[27] provide a corpus of scanned boring logs from subsurface investigations from levees, buildings, housing developments, and other infrastructure projects. We have digitized many of the scanned boring logs to develop a digital dataset that contains the date, depth, and method of sample collection; a description of the soil texture; penetration test results; fines content; and soil behavior classifications. Like the CGS dataset, we assign fines content and soil behavior classifications to samples without laboratory test data based on the samples' description and the laboratory test data from nearby samples. We also associate each sample with a specific geologic deposit based on the sample's description and proximity to mapped geologic deposits. The compiled dataset from the scanned boring logs contains 943 samples from 157 borings drilled between October 1980 and November 2006.

DWR[28] also provides data from recent infrastructure projects within the study area. The data is proprietary and cannot be published publicly, but the comprehensive dataset includes sample descriptions, penetration test data, and laboratory test data. As with the other sample datasets, we review each sample description and assign fines content and soil behavior classifications to samples without laboratory test data. We also associate each sample with one of the geologic deposits within the study area based on the samples' description, density, texture, and location relative to the mapped geologic deposits. The compiled dataset includes 945 samples from 30 borings drilled between May 2009 and September 2012.

3.4. Cone penetration test data

The USGS[29] has provided a database of cone penetration test (CPT) data within the project area. The digital files include penetration resistance, sleeve friction, and in some cases, pore pressure measurements. We process the data by identifying thin layers that can influence the CPT tip resistance and calculate a corrected tip resistance using the inversion process described by Boulanger and DeJong[30]. We have also reviewed the cone logs from each test and have assigned geologic contact elevations based on the tip resistance and soil behavior classification index in conjunction with the available geologic maps. The compiled dataset includes 545,160 samples from 169 probes.

[27] Grant, A. (2021) Personal communication.
[28] Ilankatharan, L. (2021). Personal communication.
[29] Grant, A. (2021). Personal communication.
[30] Boulanger, R.W. and DeJong, J.R. (2018). Inverse filtering procedure to correct cone penetration data for thin-layer and transition effects. Proceedings of the Cone Penetration Testing.

3.5. Subsurface data processing

3.5.1. Soil behavior classification

The available geotechnical boring data include descriptions of the soil texture, plasticity, penetration resistance, and other geotechnical characteristics at the specific sampling locations. Soil behavior classifications and fines content estimates are needed for liquefaction susceptibility and triggering analyses. We assign soil behavior classifications to samples without laboratory tests based on the sample's description and comparison with nearby samples with laboratory data. In the absence of nearby laboratory data, we assigned soil behavior classifications and fines content based on the average values from similar samples with laboratory test results. Sample records described as clay or clayey are assumed to have a plasticity index (*PI*) greater than 7 and behave as clay-like. The unit weight and fines content are similarly assigned to samples without associated laboratory tests based on the sample descriptions and correlations with nearby borings. The fines content associated with the sample descriptions is specific to each project's classification scheme. For example, Figure 3.1 shows two similar fines classification schemes for two different projects. In the complete absence of contextual information, we estimated fines content and unit weights using the guidelines provided in the CalTrans Soil and Rock Logging, Classification, and Presentation manual (Figure 3.1.b). Estimates of fines content are only needed for liquefaction triggering analyses in soils described as sand-like.

(a)

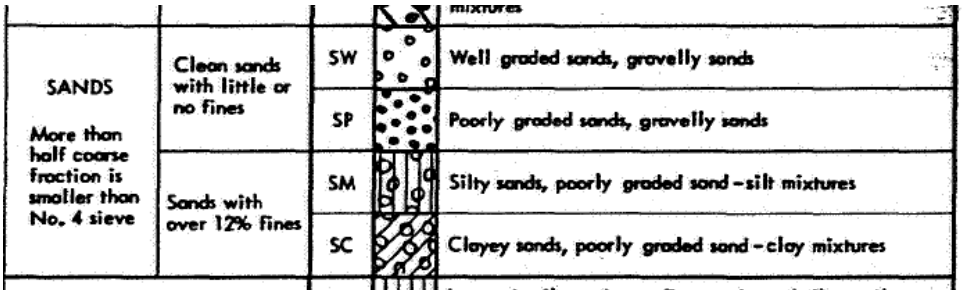

(b)

	Fines	Grade	Type of Fines	Group Symbol	Sand/Gravel	Group Name
Sand	≤ 5%	Well		SW	< 15% gravel	Well-graded SAND
					≥ 15% gravel	Well-graded SAND with GRAVEL
		Poorly		SP	< 15% gravel	Poorly-graded SAND
					≥ 15% gravel	Poorly-graded SAND with GRAVEL
	10%	Well	ML or MH	SW-SM	< 15% gravel	Well-graded SAND with SILT
					≥ 15% gravel	Well-graded SAND with SILT and GRAVEL
			CL or CH	SW-SC	< 15% gravel	Well-graded SAND with CLAY
					≥ 15% gravel	Well-graded SAND with CLAY and GRAVEL
		Poorly	ML or MH	SP-SM	< 15% gravel	Poorly-graded SAND with SILT
					≥ 15% gravel	Poorly-graded SAND with SILT and GRAVEL
			CL or CH	SP-SC	< 15% gravel	Poorly-graded SAND with CLAY
					≥ 15% gravel	Poorly-graded SAND with CLAY and GRAVEL
	≥ 15%		ML or MH	SM	< 15% gravel	SILTY SAND
					≥ 15% gravel	SILTY SAND with GRAVEL
			CL or CH	SC	< 15% gravel	CLAYEY SAND
					≥ 15% gravel	CLAYEY SAND with GRAVEL

Figure 3.1 – Examples of project-specific fines content classification schemes. (a) East Bay Municipal Utility District Levees at Aqueduct Crossing[31] (b) CalTrans borings[32]

3.5.2. Standard penetration test data

Liquefaction triggering analyses requires an overburden, energy, and fines-content-corrected penetration resistance value, $(N_1)_{60cs}$, which we have assumed based on the samples' depth, date, and drilling method. The SPT data compiled from disparate sources was collected using a variety of hammers and samplers, with a wide range of data quality. We assume SPT hammer efficiency as a function of the hammer type and the date of the investigation. Without direct energy measurements, all donut, safety, and cathead-and-rope systems are assumed to be 60% efficient. All investigations conducted before the mid-1980s are also assumed to use hammers with 60% efficiency. The National Academy of Engineering[33] indicates that modern automatic trip hammers typically have an efficiency greater than about 80% and we assume an 80% efficiency for these systems. Many of the investigations within the study area utilize non-standard California

[31] ConverseWardDavisDixon (1980). Evaluation of Levees at Aqueduct Crossings for East Bay Municipal Utility District.

[32] California Department of Transportation (2010). Soil and Rock Logging, Classification, and Presentation Manual.

[33] National Academies of Sciences, Engineering, and Medicine (2019). *Manual on Subsurface Investigations*. National Academy Press.

or modified California samplers. We correct the applied energy of oversized samplers using Burmeister's[34] energy conversion. Other correction factors include drill rod length and sampler diameter.

The processed $(N_1)_{60cs}$ values span a wide range, from 0 to over 50 blows/ft. Penetration resistance is log-normally distributed, so disregarding high blow counts in the dataset or treating them as not susceptible to liquefaction may artificially skew the distribution towards a lower median. Likewise, soils that are clay-like and not susceptible to liquefaction need to be distinguished from those that are too dense to liquefy. Some of the soils within the dataset are indeed very dense and the high blow counts do not necessarily imply blockage. Based on common field reporting practices, the maximum penetration resistance in the dataset is limited to 50 blows/ft.

3.5.3. Cone penetration test data

We also processed the CPT tip resistance to account for the influence of interbedded layers of dense and soft soils using the thin layer corrections described by Boulanger and DeJong[35]. CPT soil behavior index (I_c) values ranging from 2.4 to 2.6 are often used as a threshold to separate clay-like from sand-like soil behavior, with larger I_c values indicating clay-like behavior. While the SPT dataset includes 135 Atterberg limit tests, none of the Atterberg limit tests are collocated with CPT probes for project-specific correlations. Without data to support a lower threshold value, CPT I_c values greater than 2.6 are often assumed to exhibit clay-like behavior[36]. Samples with I_c values less than 2.6 are assumed to behave as sand-like and could be susceptible to liquefaction if they are saturated. We analyze the CPT samples deemed to be susceptible to liquefaction using the CPT-based liquefaction triggering and fines content adjustment described by Boulanger and Idriss[37] to calculate an overburden stress and fines content-corrected tip resistance, q_{c1Ncs}.

Since Boulanger and Idriss's SPT-based and CPT-based liquefaction triggering analyses are derived using independent SPT and CPT datasets, the resulting limit state functions are slightly different. For example, the fines content adjustment in the CPT procedure has a much greater influence on the liquefaction resistance compared to the SPT procedure. In current practice, there is no unified method to combine SPT and CPT data for liquefaction triggering analyses. To address the independent SPT and CPT datasets, we used the corrected CPT penetration resistance to

[34] Burmister, D.M. (1948). The importance and practical use of relative density in soil mechanics: Proceedings of ASTM, v. 48:1249.

[35] Boulanger and DeJong (2018). See note 30.

[36] Holzer, T.L., Noce, T.E., and Bennett, M.J. (2011). Liquefaction Probability Curves for Surficial Geologic Deposits. *Environmental and Engineering Geoscience*, 17(1).

[37] Boulanger, R.W. and Idriss, I.M. (2016). CPT-based liquefaction triggering procedure. *J. Geotech. Geoenviron. Eng.*, 142(2).

estimate an equivalent SPT-based penetration resistance using the equivalent relative density equations provided by Idriss and Boulanger[38], which are:

$$D_R = \sqrt{\frac{(N_1)_{60}}{46}} \tag{3.5.1}$$

$$D_R = 0.478(q_{c1N})^{0.264} - 1.063 \tag{3.5.2}$$

where D_R is the relative density, $(N_1)_{60}$ is the overburden and energy-normalized penetration resistance and q_{c1N} is the overburden-normalized penetration resistance.

3.5.4. Subsurface database summary

With the combined datasets, we apply the fines content adjustments and calculate the lognormal median and standard deviation of the $(N_1)_{60cs}$ penetration resistance for the liquefaction susceptible soils for each independent geologic deposit. Each sample was weighted based on its representative measurement interval, with SPT measurements weighted based on a 0.45 m penetration interval and CPT measurements weighted based on a 0.05 m penetration interval. Table 3.1 lists the weighted fraction of soils that are susceptible to liquefaction when saturated and the median and lognormal standard deviation of $(N_1)_{60cs}$ for each soil deposit.

Table 3.1: Soil deposit weighted statistics

Soil deposit	Fraction susceptible when saturated	Median $(N_1)_{60cs}$ of susceptible soils	Lognormal standard deviation, $\sigma_{ln\ N}$
Af	0.62	8.3	0.819
Qha	0.37	12.6	0.820
Qhc	0.44	14.0	0.694
Qhm	0.15	7.5	0.767
Qd	0.84	22.0	0.820
Qp	0.57	38.6	0.621

For site-specific investigations, Boulanger and Idriss' equations[39,40] imply that the lognormal standard deviation of $(N_1)_{60cs}$ is 0.15 and q_{c1Ncs} is 0.20. Table 3.1 shows that uncertainty associated with $(N_1)_{60cs}$ of the liquefaction susceptible soils is much greater for an entire geologic deposit. The deposit-scale lognormal standard deviation ranges from about 0.62 in the relatively dense Qp deposit to over 0.82 in the highly variable fill (Af) and Qha deposits. The increased

[38] Idriss, I.M. and Boulanger, R.W., 2008. Soil liquefaction during earthquakes. Earthquake Engineering Research Institute.

[39] Boulanger, R.W. and Idriss, I.M. (2012). Probabilistic standard penetration test–based liquefaction–triggering procedure. *J. Geotech. Geoenviron. Eng.*, 138(10), pp.1185-1195.

[40] Boulanger and Idriss (2016). See note 37.

standard deviation leads to highly uncertain estimates of penetration resistance if only average deposit-scale statistics are considered.

The combined datasets of the DWR well completion reports, monitoring wells, and CGS borehole data include over 5,400 groundwater observations from September 1962 to October 2020. The combined datasets of the CGS boreholes, DWR scanned logs, and DWR proprietary information provides over 6,300 SPT samples. The USGS CPT dataset also provides over 545,160 CPT samples. The combined datasets of CGS, DWR scanned logs, DWR proprietary information, USGS CPT, and Atwater data provide a comprehensive lithology dataset of over 556,600 samples. Table 3.2 provides a listing of the datasets. Figure 3.2 shows the spatial distribution of the subsurface investigations within the study area.

Table 3.2: Subsurface metadata

Source	Data	Number of investigations	Number of samples
DWR Well completion records	Groundwater	370	370
DWR monitoring well	Groundwater	56	4,581
CGS boreholes	Groundwater	464	464
CGS boreholes	Lithology, soil behavior, and SPT	805	4,427
DWR scanned logs	Lithology, soil behavior, and SPT	157	943
DWR proprietary	Lithology, soil behavior, and SPT	30	945
USGS CPT	Lithology, soil behavior, and CPT	169	545,160
Atwater	Lithology	654	4,676

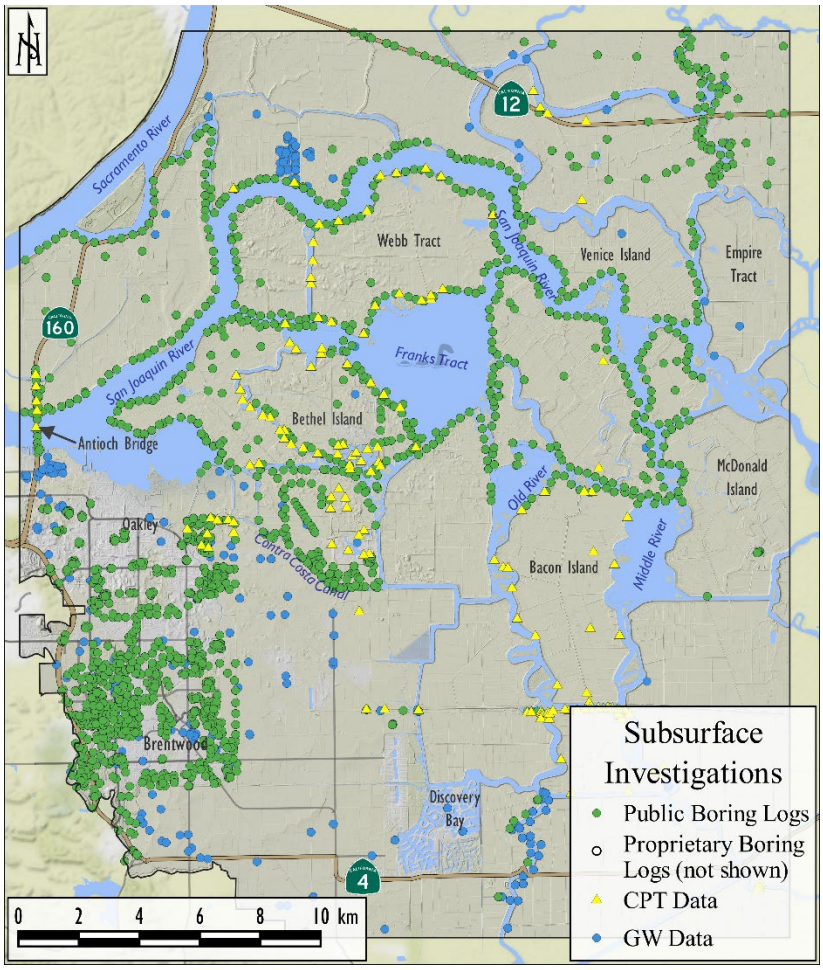

Figure 3.2 – Spatial distribution of subsurface investigations

We generate ESRI shapefiles of the publicly-available groundwater data, SPT penetration resistance, and CPT penetration resistance for subsequent liquefaction analyses. The shapefiles providing SPT and CPT data also provide elevation data, lithology, and soil behavior classifications. All shapefiles are referenced to the WGS 84 / UTM Zone 10N (EPSG: 32610) coordinate system, with elevation in NAVD88 (m). The shapefiles may be accessed via the DesignSafe portal at https://www.designsafe-ci.org/data/browser/public/designsafe.storage.published/PRJ-3406.

4. Liquefaction analysis methodology

Geotechnical engineers usually analyze liquefaction hazards by a sequential evaluation of:

1. The soil's susceptibility to liquefaction,
2. The probability liquefaction will trigger given an estimate of the cyclic stresses induced by an earthquake, and then

3. The consequences of liquefaction based on the soil layer thicknesses, depths, factors of safety, topography, hydraulic conductivity, and other subsurface factors.

The specific criteria and procedures for each of these steps depend upon the scope and size of the area concerned, and whether a significant amount of subsurface data is available. These differing approaches are explained in the following sections.

4.1. Site-specific liquefaction susceptibility, triggering, and manifestation analyses

4.1.1. Susceptibility

For significant pore water pressure to be generated, soils must be saturated or very nearly saturated. Liquefaction susceptibility also depends on the soil's composition. The soil's plasticity index, *PI*, is commonly used to assess liquefaction susceptibility. Boulanger and Idriss[41] recommend a simple, upper bound guideline of saturated soils with $PI < 7$ behave as "sand-like" and may be susceptible to liquefaction. Although clay soils may soften during shaking, they do not liquefy in the same manner as clean, uniformly graded, loose granular soils.

While the criteria developed by Bray and Sancio[42] are sometimes used to identify liquefaction susceptibility, their criteria use the ratio of water content to liquid limit as a function of liquefaction susceptibility. The water content of saturated soils is a function of relative density, which is also related to cyclic resistance. Including water content as part of the liquefaction susceptibility criteria may artificially shift the distribution of cyclic resistance towards lower values. Also, water content is a transient property; soils that are not saturated with low water content at the time of exploration may become saturated with increasing water content during wet periods. For these reasons, the Bray and Sancio criteria are not utilized for this project.

4.1.2. Liquefaction triggering

Once susceptible soils have been identified, the next step is to determine the probability that liquefaction will be triggered when subjected to sufficiently strong shaking. To compute probabilities of liquefaction triggering, we adopt a modified version of the simplified liquefaction triggering procedure first described by Seed and Idriss[43] and later updated by Boulanger and Idriss.[44,45] This simplified procedure considers soils likely to liquefy if the cyclic stress ratio (*CSR*) exceeds the cyclic resistance ratio (*CRR*). In the simplified method, the *CSR* is estimated based on the peak ground acceleration (*PGA*), vertical total and effective stress (σ_v and σ_v'), and layer depth. A shear stress reduction factor (r_d) accounts for the dynamic response of the soil profile during

[41] Boulanger, R.W. and Idriss, I.M. (2006). Liquefaction susceptibility criteria for silts and clays. *J. Geotech. Geoenviron. Eng.*, 132(11).

[42] Bray, J.D. and Sancio, R.B. (2006). Assessment of the liquefaction susceptibility of fine-grained soils. *J. Geotech. Geoenviron. Eng.*, 132(9), pp.1165-1177.

[43] Seed and Idriss (1971)

[44] Boulanger and Idriss (2012). See note 39.

[45] Boulanger and Idriss (2016). See note 37.

shaking. Laboratory tests also indicate that the number of cycles of loading and the overburden pressure affect liquefaction triggering behavior. In current practice, the *CSR* is adjusted for overburden stress and ground motion duration using an overburden correction factor (K_σ) and an earthquake magnitude scaling factor (*MSF*).

The resistance to cyclic loading (*CRR*) is typically estimated as a function of SPT or CPT results. Field penetration measurements are adjusted for factors such as fines content, overburden pressure, and hammer energy to produce an equivalent penetration resistance to represent standard conditions. Estimates of *CRR* based on this equivalent resistance can include significant uncertainty due to variability in site conditions, testing equipment, and sampling procedures. The results of these analyses are often expressed as a probability of liquefaction triggering using a normally distributed limit state function, rather than a binary "yes or no" outcome.

Given the large uncertainties in soil liquefaction cyclic stress and resistance parameters, the simplified triggering procedure has been reformulated as a limit state function, g, which Boulanger and Idriss (2012) define as:

$$g = ln\, R - ln\, S \tag{4.1.1}$$

where R is a random variable for cyclic resistance ratio and S is a random variable for cyclic stress ratio. Boulanger and Idriss assume that the resistance and loading variables, R and S, are independent log-normally distributed random variables and liquefaction is likely if $g < 0$. They define the cyclic resistance ratio, R, as:

$$lnR = \left(\left[\frac{N}{14.1} + \left(\frac{N}{126}\right)^2 - \left(\frac{N}{23.6}\right)^3 + \left(\frac{N}{25.4}\right)^4 - 2.67\right] + \varepsilon_{lnR}\right) \tag{4.1.2}$$

where N is the mean depth, energy, overburden, and fines-corrected SPT penetration resistance, also denoted $(N_1)_{60cs}$, and ε_{lnR} is a random variable to account for model uncertainty in cyclic resistance ratio with zero mean and variance ${\sigma_{ln\,R}}^2$. The soil's $(N_1)_{60cs}$ penetration resistance is typically assumed to be normally distributed with a constant coefficient of variation. This quantity is equivalent to a constant log-normal standard deviation, such that:

$${COV_N}^2 = e^{{\sigma_{\ln N}}^2} - 1 \tag{4.1.3}$$

where COV_N is the coefficient of variation and $\sigma_{\ln N}$ is the lognormal standard deviation.

Since the uncertainty in groundwater elevation must also be considered, we expand the Boulanger and Idriss (2012) formulation for cyclic stress ratio, *S*, to allow for the inclusion of a random variable accounting for the uncertainty in groundwater depth. The cyclic resistance ratio, *S*, is therefore computed at a particular depth *z* as:

$$ln\, S = ln\left(0.65\, PGA\, r_d\, \frac{1}{MSF}\frac{1}{K_\sigma}\right) + ln\left(\frac{\sigma_v}{\sigma_v - \gamma_w[z - \hat{z}_w - \varepsilon_z]}\right) + \varepsilon_{ln\,S} \tag{4.1.4}$$

where *PGA* is the input peak ground acceleration, r_d is the stress reduction factor, *MSF is* the magnitude scaling factor, K_σ is the effective overburden stress correction factor, z is the depth of interest, $\hat{z}_w$ is the mean estimated groundwater depth, and ε_z is a normally-distributed random variable with a mean of zero and a variance of ${\sigma_{z_w}}^2$ to account for the uncertainty in groundwater depth. Equation (4.1.4) is valid only where soils are saturated, the groundwater level is above the depth of interest, $z - \hat{z}_w > 0$, and the pore pressure is hydrostatic.

To estimate the uncertainty in liquefaction triggering, we use equations (4.1.2) and (4.1.4) to calculate the mean values of the limit state function, g. Assuming that penetration resistance is log-normally distributed, the first-order second-moment approximation of the limit state function variance, ${\sigma_T}^2$, is:

$$ {\sigma_T}^2 = \left[\frac{\widehat{N}}{14.1} + 2\left(\frac{\widehat{N}}{126}\right)^2 - 3\left(\frac{\widehat{N}}{23.6}\right)^3 + 4\left(\frac{\widehat{N}}{25.4}\right)^4\right]^2 (\sigma_N)^2 + \left[\frac{\gamma_w}{\sigma_v - \gamma_w \max[z-\hat{z}_w, 0]}\right]^2 \left(\sigma_{z_w}\right)^2 + (\sigma_{ln\,R})^2 + (\sigma_{ln\,S})^2 \quad (4.1.5) $$

4.1.3. Liquefaction ground damage

The susceptibility criteria and simplified triggering procedures identify layers of soil that could liquefy during an earthquake, but additional analyses are still needed to identify situations that could result in ground surface manifestation and damage. For example, liquefied soil at depth does not always result in ground damage, so the consequences of liquefaction may be less severe if liquefaction is triggered only at great depths. Ishihara[46] proposed simple, but widely used, empirically-based curves that separate case histories of ground surface damage from case histories where damage was not observed. Figure 4.1 shows the curves separating the case histories, which we approximate using the equations:

$$ {H_1}^* = 0.090\, H_1 \left(\frac{PGA}{1\text{ g}}\right)^{-1.496} \quad (4.1.6) $$

$$ H_2 = {H_1}^* \left[1 + \exp\left(\frac{{H_1}^* - 3.33\text{ m}}{0.515\text{ m}}\right)\right] \quad (4.1.7) $$

where ${H_1}^*$ is adjusted crust thickness, H_1 is the non-liquefied surface crust thickness, *PGA* is the peak ground acceleration at the ground surface, and H_2 is the minimum thickness of liquefied soil that would result in the ground surface manifestation of liquefaction.

[46] Ishihara, K. (1985). Stability of natural deposits during earthquakes. Proc. 11th Int'l Conf on Soil Mechanics and Foundation Engineering.

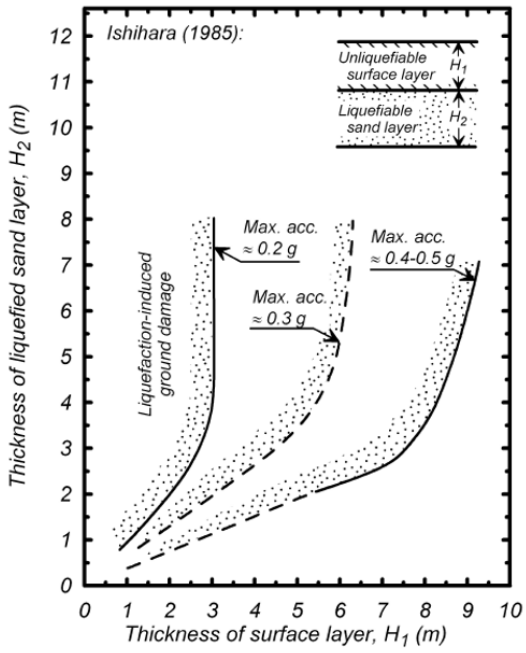

Figure 4.1. Liquefaction ground manifestation curves (from Ishihara)

In addition to the curves in Figure 4.1, multiple semi-empirical procedures are available to calculate the probability of liquefaction ground damage based on SPT or CPT data. Geyin and others[47] describe liquefaction ground damage fragility functions for engineering damage parameters including liquefaction potential index (*LPI*) and an Ishihara curve-inspired variant (LPI_{Ish}). These parameters are computed based on the factor of safety against liquefaction, which does not account for the increased uncertainty in cyclic resistance at a deposit scale. Consequently, we only utilize *LPI* and its variants for site-specific analyses in this study.

4.2. Deposit-scale liquefaction analyses

Site-specific liquefaction analyses require measurements of the groundwater table, the soil's plasticity index, and penetration resistance to estimate the probability of liquefaction. Unfortunately, such subsurface properties are rarely well-defined for a whole region or sometimes even for a specific project. Many past studies[48,49] have relied on descriptions of the ground surface soils and geology to approximate the subsurface conditions at locations without subsurface data. More recent studies[50] have assigned probabilistic random variables to subsurface properties like groundwater depth, soil behavior classification, and penetration resistance based on

[47] Geyin, M., Baird, A.J. and Maurer, B.W., 2020. Field assessment of liquefaction prediction models based on geotechnical versus geospatial data, with lessons for each. Earthquake Spectra, 36(3), pp.1386-1411.
[48] Youd et al. (1978). See note 4.
[49] Witter et al. (2006). See note 16.
[50] Real and Knudsen (2010). See note 5.

comprehensive boring datasets. Greenfield and others[51] demonstrate that estimates based on a large boring dataset in Portland, Oregon approximate site-specific liquefaction susceptibility, triggering, and deformation analyses much better than methods based on surface geology alone. Holzer and others[52] demonstrate that liquefaction analyses using a large subsurface dataset reasonably estimate the probability of liquefaction in fill and alluvial deposits following the 1989 M6.9 Loma Prieta earthquake.

To address the increased uncertainty for deposit-scale analyses, we extend Boulanger and Idriss's[53] site-specific liquefaction triggering equations by including random variables for groundwater depth, soil behavior classification, and penetration resistance. The site-specific liquefaction triggering equations assume that groundwater and liquefaction susceptibility characteristics are known and are scalar values. However, these values are uncertain at the scale of a geologic deposit and must be treated as random variables. This probabilistic extension greatly increases the uncertainty in the liquefaction triggering and deformation estimates but is necessary for deposit-scale approximations. By addressing the uncertainty in groundwater table depth, soil behavior classification, and penetration resistance, the probability of liquefaction within a geologic deposit may be defined as:

$$P[liq] = P[sat]P[sand]P[CSR > CRR|sand] \quad (4.2.1)$$

where $P[liq]$ is the probability of liquefaction, $P[sat]$ is the probability the soil is saturated, $P[sand]$ is the probability that the soil layer exhibits sand-like behavior and is susceptible to liquefaction when saturated, and $P[CSR > CRR|sand]$ is the probability of $CSR > CRR$. Greenfield and Grant[54] described additional details about the probabilistic extension of site-specific liquefaction triggering methods for deposit-scale analyses.

The comprehensive subsurface boring and well log database can be used to estimate the range of subsurface properties within a geologic deposit and develop statistics for regional-scale liquefaction hazard analyses. Liquefaction susceptibility analyses require each soil layer to be classified as either sand-like or clay-like. *PI* data and soil descriptions from a boring dataset can be used to estimate the probability of encountering a sand-like soil layer within a particular geologic deposit. Comprehensive boring log databases with penetration tests and gradation results can also be used to estimate the distribution of $(N_1)_{60cs}$ values within a geologic deposit. The statistics associated with the depth of groundwater, soil behavior classification, and penetration resistance for each deposit may then be incorporated into equation (4.2.1) to calculate $P[sat]$, $P[sand]$, and $P[CSR > CRR|sand]$.

Just like soil behavior classification, the geologic deposit at any location may also be uncertain. Invoking the total probability theorem and assuming that the soil behavior properties

[51] Greenfield et al. (2018). See note 6.
[52] Holzer et al. (2011). See note 36.
[53] Boulanger and Idriss (2012). See note 39.
[54] Greenfield and Grant (2020). See note 7.

within each geologic deposit are independent of other geologic deposits, including the uncertainty in geologic deposits at any location yields:

$$P[liq] = P[sat] \sum_{geo} P[geo] P[sand|geo] P[CSR > CRR|sand, geo] \quad (4.2.2)$$

where $P[geo]$ is the probability the soil at any location is a member of geologic deposit geo.

The semi-empirical methods for liquefaction triggering[55] use overburden and fines-corrected penetration resistance from SPT boring or CPT probe investigations to calculate a cyclic resistance ratio, *CRR*. In the site-specific analyses, the uncertainty in *CRR* is addressed by summing the individual components of variance for each input parameter (such as penetration resistance, fines content, and model uncertainty) via algebraic or first-order-second-moment approximation. Greenfield and Grant[56] showed that these input properties become highly uncertain for deposit-scale analyses where subsurface investigations are limited.

Site-specific analyses for consequences of liquefaction can also be extended for deposit-scale analyses with some adjustments. Liquefaction at depth does not necessarily produce ground damage, and the curves developed by Ishihara[57] may be used to identify conditions where ground damage may occur. In shallow, thick, liquefiable deposits, liquefaction is very likely to produce ground surface deformation. In such conditions, the probability of ground damage is approximately equal to the probability of liquefaction triggering. However, in deep or thin liquefiable deposits, the probability of ground deformation at the surface may be significantly less than the probability of liquefaction triggering.

Equations (4.1.5) and (4.1.6) provide an estimate of the minimum thickness of liquefied soil (H_2) below a non-liquefied crust (H_1) necessary to produce ground damage. Equation (4.2.2) provides a method to calculate the probability of liquefaction at a specific depth. To estimate the probability of liquefaction ground damage, we calculate the joint probability of liquefaction at both the top and bottom of layer H_2, such that:

$$P[L] = P[liq_{H_1}] P\left[liq_{H_1+H_2} | liq_{H_1}\right] \quad (4.2.3)$$

where $P[L]$ is the probability of liquefaction ground damage, $P[liq_{H_1}]$ is the probability of liquefaction at the top of the liquefiable layer, and $P\left[liq_{H_1+H_2} | liq_{H_1}\right]$ is the conditional probability of liquefaction at the bottom of the liquefiable layer. The thicknesses H_1 and H_2 are calculated using equations (4.1.5) and (4.1.6). Since the soil must be saturated at depth H_1 for liquefaction to be triggered, the conditional probability of liquefaction at depth $H_1 + H_2$ is:

[55] E.g., Boulanger and Idriss (2012), see note 39; Boulanger and Idriss (2016), see note 37.
[56] Greenfield and Grant (2020). See note 7.
[57] Ishihara (1985). See note 46.

$$P\left[liq_{H_1+H_2}|liq_{H_1}\right] = \sum_{geo} \begin{matrix} P[geo]P\left[sand_{H_1+H_2}|sand_{H_1}, geo\right] \cdot \\ P\left[CSR > CRR_{H_1+H_2}|CSR > CRR_{H_1}, sand_{H_1+H_2}, geo\right] \end{matrix} \quad (4.2.4)$$

where $P\left[sand_{H_1+H_2}|sand_{H_1}, geo\right]$ is the conditional probability of encountering sand-like soils at the bottom of the liquefiable layer and $P\left[CSR > CRR_{H_1+H_2}|CSR > CRR_{H_1}, sand_{H_1+H_2}, geo\right]$ is the conditional probability of the *CSR* being greater than the *CRR* at the bottom of the liquefiable layer. Assuming that the probabilities of liquefaction at each depth are derived from a latent normally distributed limit state function (i.e., the assumptions from Boulanger and Idriss[58]), the conditional probabilities in equation (4.2.4) may be calculated using approximations for bivariate normal distributions[59], such that:

$$a = \Phi^{-1}(P[CSR > CRR_{H_1}|sand_{H_1}, geo]) \quad (4.2.5)$$

$$b = \Phi^{-1}(P[CSR > CRR_{H_1+H_2}|sand_{H_1+H_2}, geo]) \quad (4.2.6)$$

$$P\left[CSR > CRR_{H_1+H_2}|CSR > CRR_{H_1}|sand_{H_1}, geo\right] = \Phi\left(\frac{\frac{\rho_{a,b}\phi(-a)}{\Phi(-a)}+b}{\sqrt{1+{\rho_{a,b}}^2}}\right) \quad (4.2.7)$$

where a and b are intermediate values that represent latent mean values of the standard normal distribution, Φ is the standard normal cumulative density function, ϕ is the standard normal probability density function (the derivative of Φ), and $\rho_{a,b}$ is the correlation coefficient between a and b. Expressions for $P\left[sand_{H_1+H_2}|sand_{H_1}, geo\right]$ may be defined similarly. The unconditional probabilities of $CSR > CRR$ at depths H_1 and $H_1 + H_2$ are readily calculated using equations (4.1.6) and (4.1.7) defined in the previous section. To calculate the conditional probability at $H_1 + H_2$, we define $\rho_{a,b}$ using an arbitrary geospatial function, for example, the Gaussian radial basis function:

$$\rho_{a.b} = \exp\left(-\frac{{H_2}^2}{2s^2}\right) \quad (4.2.8)$$

where H_2 is the distance between the depths of the CRR estimates and s is a length scaling factor. Figure 4.2 shows the correlation coefficient between CRR observations at a depth of 2 m (H_1) and other arbitrary depths ($H_1 + H_2$). When H_2 is small relative to s, $\rho_{a.b}$ approaches 1.0 and the conditional probability of $CSR > CRR$ at $H_1 + H_2$ approaches 1.0. Conversely, as H_2 becomes large relative to s, $\rho_{a.b}$ approaches 0 and the probability of $CSR > CRR$ at $H_1 + H_2$ is uncorrelated from observations at H_1. The resulting lack of correlation results in a conditional probability of $CSR > CRR$ at $H_1 + H_2$ that may be less than 1.0, decreasing the probability of liquefaction.

[58] Boulanger and Idriss (2012), see note 39; Boulanger and Idriss (2016), see note 37.

[59] Cox, D.R. and Wermuth, N. (1991). A simple approximation for bivariate and trivariate normal integrals. *International Statistics Review*. 59(2).

Together, Figures 4.1 and 4.2 imply that liquefaction of deeper and thinner layers is less likely to result in ground damage than liquefaction of near-surface or thicker soil layers.

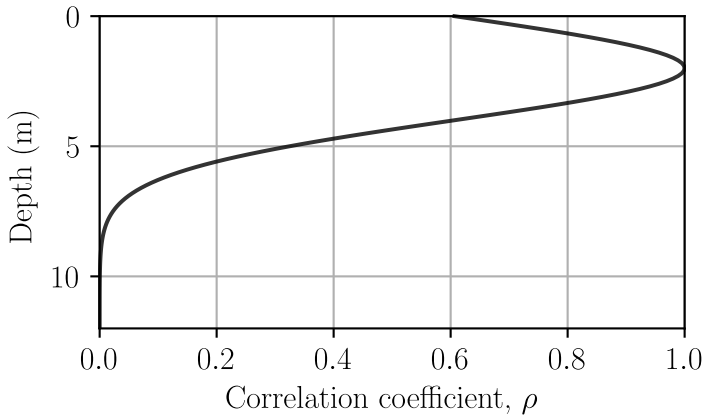

Figure 4.2. The correlation coefficient for $CSR > CRR$ at arbitrary depths given $CSR > CRR$ at a depth of 2 m. A length scaling factor (s) of 2 m is assumed.

4.3. Spatial interpolation of subsurface properties

The geologic deposit summary (Table 3.1) indicates the soil behavior classification and penetration resistance of an entire geologic deposit include a great amount of uncertainty. When performing analyses for a large area, localized site-specific data should be used wherever possible but the analyses should approach deposit-scale averages where limited data are available. This section discusses how the site-specific and deposit scale liquefaction analyses may be unified while accounting for the uncertainty at any given location.

The uncertainty in subsurface properties, such as penetration resistance, increases with distance from the sample locations. For example, Figure 4.3 shows a log-normal variogram of 1,234 corrected penetration resistance measurements, $(N_1)_{60cs}$, as a function of the distance between samples in a dune sand (Qd) soil deposit. At zero distance between samples, the variance approaches the spatially independent variance or measurement uncertainty (nugget). The variance increases with the distance between samples to a point (the range) beyond which samples are no longer spatially correlated. The variance beyond the range approximates the marginal variance of the entire dataset (the sill).

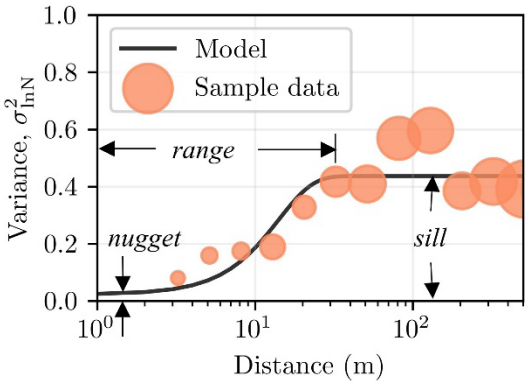

Figure 4.3. Variogram for $(N_1)_{60cs}$ penetration resistance from a database of dune sand soils. The circle size represents the relative number of samples within each bin.

A Gaussian process (GP) provides a robust method to model the spatial correlation of data and interpolate between observation locations. The GP model relies on a separable kernel function to define the covariance between observation locations, such that:

$$\widehat{\boldsymbol{K}}_{ij} = \kappa\left(\widehat{\boldsymbol{X}}_i, \widehat{\boldsymbol{X}}_j\right) = {\sigma_y}^2 \, exp\left(-\frac{\|\widehat{\boldsymbol{X}}_i - \widehat{\boldsymbol{X}}_j\|^2}{2s^2}\right) + \delta_{ij}{\tau_y}^2 \tag{4.3.1}$$

where $\widehat{\boldsymbol{K}}_{ij}$ is the i,j^{th} component of the normalized covariance matrix; κ is a separable kernel function; ${\sigma_y}^2$ is the spatial variance of the Gaussian process; s is an influence length parameter; δ_{ij} is the Kronecker delta; ${\tau_y}^2$ is the variance of the measurement uncertainty; and the expression $\|\widehat{\boldsymbol{X}}_i - \widehat{\boldsymbol{X}}_j\|$ is the Euclidean distance between locations i and j. The predicted value of the GP at any arbitrary location (x) is a normally distributed random variable with mean and variance:

$$y(x) = \mathcal{N}\left(\mu(x), \sigma^2(x)\right) \tag{4.3.2}$$

$$\mu(x) = \boldsymbol{K}_* \widehat{\boldsymbol{K}}^{-1} \widehat{\boldsymbol{y}} \tag{4.3.3}$$

$$\sigma^2(x) = {\sigma_y}^2 + {\tau_y}^2 - {\boldsymbol{K}_*}^T \widehat{\boldsymbol{K}}^{-1} \boldsymbol{K}_* \tag{4.3.4}$$

where $y(x)$ is the normally-distributed $(\mathcal{N})$ GP estimator, $\mu(x)$ is the mean of the GP at x, $\widehat{\boldsymbol{y}}$ is a vector of normalized data observations, $\sigma^2(x)$ is the variance of the GP at x, $\boldsymbol{K}_* = \kappa\left(x, \widehat{\boldsymbol{X}}_j\right)$, and ${\boldsymbol{K}_*}^T$ is the transpose of $\boldsymbol{K}_*$. The model hyperparameters (σ_y, τ_y, and s) are fit to the observed data using maximum likelihood optimizations. Rasmussen and Williams[60] calculate the log marginal likelihood of the Gaussian process fitting the data as:

$$ln\, P\left[\widehat{\boldsymbol{y}}|\widehat{\boldsymbol{X}}\right] = \frac{1}{2}\widehat{\boldsymbol{y}}^T \widehat{\boldsymbol{K}}^{-1} \widehat{\boldsymbol{y}} - \frac{1}{2} ln\left|\widehat{\boldsymbol{K}}\right| - \frac{n}{2} ln\, 2\pi \tag{4.3.5}$$

[60] Rasmussen, C.E. and Williams, C.K.I. (2006). Gaussian Processes for Machine Learning. MIT Press.

where $|\widehat{\boldsymbol{K}}|$ is the trace of $\widehat{\boldsymbol{K}}$ and n is the number of samples. The unknown Gaussian process model variables, ${\sigma_y}^2$, s, ${\tau_y}^2$, and s_v, are referred to as hyperparameters and can be optimally selected to maximize the log marginal likelihood of the Gaussian process model fitting the data. Using a fitted model, GP estimation, or kriging, then produces the best linear unbiased estimator of a geostatistical variable which could be groundwater depth, soil behavior classification, or soil penetration resistance[61]. For example, Figure 4.3 also shows the variance of a GP model trained to maximize the likelihood of fitting the data.

Since Gaussian processes produce normal distributions of *y*, observations in natural coordinate systems, $\widetilde{\boldsymbol{y}}$, are usually standardized to produce $\widehat{\boldsymbol{y}}$, which has an expected value of zero and a variance of one. Distributions of *y* in a standardized coordinate system can then be inverse transformed back into the natural coordinate system if additional calculations are necessary. Likewise, natural geospatial coordinates are often in dimensions in northing and easting or UTM coordinates, and these coordinates should be translated such that the means of the translated coordinates are zero.

Estimates from GP models are unbiased, normally distributed random variables that are readily converted to the probabilities of exceeding some threshold value, for example, the probability of *CSR* exceeding *CRR*. The normal distributions from GP models can also be useful to represent the observed residuals compared to a physical model, for example, the phreatic head elevation observed in wells compared to a physical groundwater model.

The hyperparameters of GP models are also very flexible, allowing for varying range scales and anisotropy factors to account for different spatial or temporal dimensions. Differences in vertical and horizontal influence lengths derived from the data can be preserved with an anisotropy factor, s_v, to scale the vertical coordinates. We transform the natural coordinates of the data, $\widetilde{\boldsymbol{X}}$, with a scaling matrix, $\boldsymbol{v}$, to account for soil anisotropy such that:

$$\widehat{\boldsymbol{X}} = \left(\widetilde{\boldsymbol{X}} - \boldsymbol{\Delta\tilde{x}}\right)\boldsymbol{v} \tag{4.3.6}$$

where $\boldsymbol{\Delta\tilde{x}}$ is a 3-component vector of the mean values of $\widetilde{\boldsymbol{X}}$ and $\boldsymbol{v} = \boldsymbol{1} + s_v\boldsymbol{u}$, where $\boldsymbol{1}$ is the three-dimensional identity matrix, s_v is the vertical anisotropic scaling factor, and $\boldsymbol{u}$ is the vertical unit vector. The value s_v can be fit to the data as an additional hyperparameter in the optimization process. A large value of s_v indicates the deposit is highly anisotropic with horizontal bedding planes exhibiting strong correlation, whereas an s_v value of one indicates isotropy and no preferential bedding.

Fitting the hyperparameters of the GP model is typically performed by optimizing the log-marginal likelihood of the model, which requires linear algebra operations on the dense covariance matrix ($\widehat{\boldsymbol{K}}$) with n^2 operations, where *n* is the number of data observations. These dense matrix

[61] Dawson, K.M., and Baise, L.G. (2005). "Three-dimensional liquefaction potential analysis using geospatial interpolation." *Soil Dynamics and Earthquake Engineering*, 25.

operations can prohibit GP calculations on conventional computers. However, recent advancements in machine learning[62] have allowed approximations of the full GP covariance matrix with much more efficient operations, which we utilize for our analyses.

Sample-specific nugget variances can be specified a priori for variable quality data (e.g., CPT versus SPT samples). However, maximum likelihood optimization has important implications for the spatial interpolation of variables. Figure 4.4 provides a comparison of two GP estimates. Figure 4.4(a) shows a GP estimate with an artificially low nugget value selected a priori. Figure 4.4(b) shows a GP estimate with a maximum likelihood-optimized nugget value. The artificially low nugget GP performs excellent at interpolating the data but provides a poor representation of the true function and its variance. The optimized GP performs better at estimating the true function, but the GP mean value tends to reflect the average of the data over the length scale.

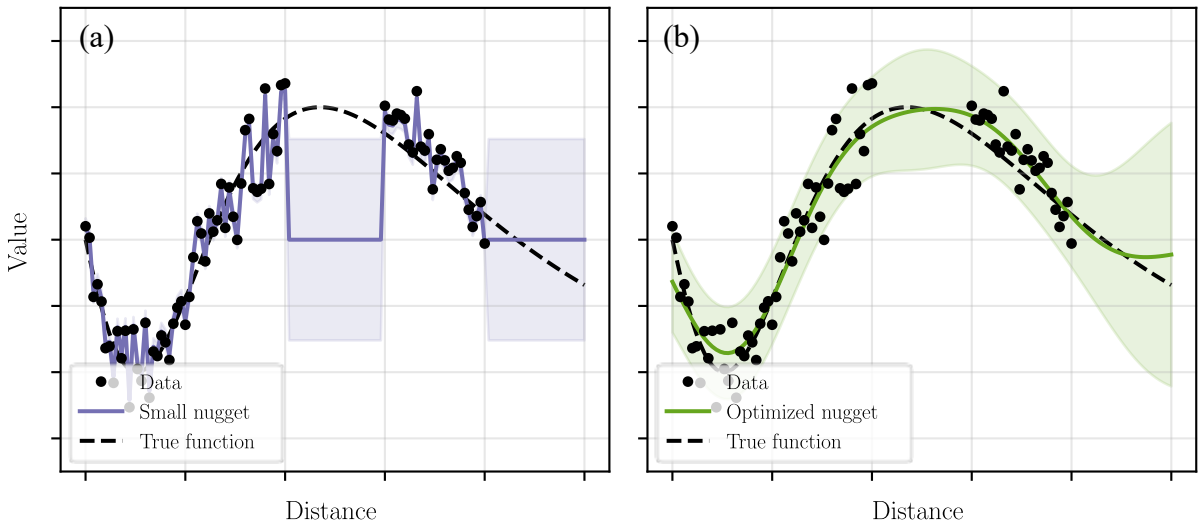

Figure 4.4. Comparison of (a) GP estimates with an artificially low nugget value and (b) optimized maximum likelihood nugget value

The random variables produced by GP models can also be transformed into classification models for applications such as geologic deposit interpolation. This is typically performed by linking a continuous GP regression model ($y(x)$ in equation 4.3.2) with a classification function. For example, the mean values from a vector of m independent GPs may be transformed from a continuous-valued vector to a probability of classification using the robust max transformation:

[62] Matthews, A.G.D.G., Van Der Wilk, M., Nickson, T., Fujii, K., Boukouvalas, A., León-Villagrá, P., Ghahramani, Z., and Hensman, J. (2017). "GPflow: A Gaussian Process Library using TensorFlow." *J. Mach. Learn. Res.*, 18(40).

$$P[c] = \begin{cases} 1-\varepsilon & c = \text{argmax}_c\, \boldsymbol{\mu} \\ \frac{\varepsilon}{m-1} & \text{otherwise} \end{cases} \tag{4.3.7}$$

where P[c] is the probability that a sample belongs to class c, ε is the assumed rate of misclassification, and $\boldsymbol{\mu}$ is a vector of the mean of m latent GP models.

The scalability and flexibility of GPs facilitate the analysis of regional-scale liquefaction with large datasets by effectively generating spatial fields of the subsurface properties that are needed for site-specific liquefaction analyses. Liquefaction analyses can then be computed at any location within the domain with the explicit characterization of the uncertainty between investigation locations. Finally, random realizations may be drawn from the GP distributions, which are useful to evaluate the spatial extent of ground damage for various scenarios. Such flexible properties are needed to evaluate the spatial distribution of groundwater, geologic deposits, soil behavior classifications, and penetration resistance.

5. Groundwater modeling

While certain geologic units can contain soil layers that are susceptible to liquefaction, the probability of liquefaction-related ground damage depends on the intensity of localized ground shaking, groundwater depth, and local topographic conditions. In particular, determining the depth and thickness of saturated liquefiable soil deposits is essential to estimate the potential for liquefaction ground damage. As such, a groundwater model that accurately represents both the available well observations and the known, physical behavior of groundwater flowing through a porous is a critical first step towards the development of a regional liquefaction hazard model.

5.1. Physical model

Fan and others[63] have developed a 1 km resolution groundwater model to estimate the water table depth for the entire planet. We first warp and align the coarse 1 km model with the Lidar-derived DEM described in Section 2.1. We then calculate a 1 km grid of groundwater elevation head and resample the groundwater elevation to match the 3 m DEM using B-Spline interpolation. The resampled global groundwater elevation model includes many locations that conflict with surface observations of canals, rivers, and irrigation ditches where surface water is visible. Likewise, the resampled global model also includes many locations where ponded water is predicted at locations of reclaimed land which are likely maintained through pumping.

To rectify the surface water observations with the resampled global model, we use a finite difference algorithm[64] with Dirichlet (fixed head) conditions at locations with observed surface

[63] Fan, Y., Li, H. and Miguez-Macho, G. (2013). "Global patterns of groundwater table depth." *Science*, 339(6122), 940-943.

[64] Wang, H.F. and Anderson, M.P. (1995). *Introduction to groundwater modeling: finite difference and finite element methods*. Academic Press.

water. We identify surface water locations using the polygons from the USGS National Map's National Hydrography Dataset[65]. We also assume fixed head conditions along the boundaries of the model to be consistent with the global groundwater model. Groundwater is assumed to flow through a 2D unconfined aquifer with Dupuit assumptions and the resampled global model is set as the initial conditions in the finite-difference algorithm. We also assume that groundwater extraction (pumping) maintains the phreatic groundwater elevation at or below the Lidar-based ground surface. Following the methods described by Fan and others, we fix the groundwater head to the ground surface at locations where the phreatic groundwater lies above the ground surface. We cycle the finite difference algorithm until the maximum phreatic elevation difference within the study area is less than 0.001 m, requiring about 10,000 iterations.

5.2. Spatial interpolation of physical model residuals

The resulting finite difference physics-based groundwater model conforms to surface water observations and the larger groundwater regime but exhibits some differences compared to the 5,415 shallow well observations. The residuals between the physical model and the wells vary in both space and time, so we trained a stochastic variational GP model with two spatial dimensions (Northing and Easting) and one temporal dimension (time before January 1, 2021) to account for the spatial and temporal variability. The covariance matrix of the data becomes computationally intractable with large datasets, so we use the sparse variational Gaussian process package GPFlow[66] in Python 3.9, which represents the dense covariance matrix as a smaller dense matrix of inducing variables. We trained a stochastic variational Gaussian process using GPFlow with about 580 inducing points, thereby reducing the computational effort and facilitating faster convergence. After fitting the hyperparameters, we reset the length scales of the two spatial dimensions as equal and continued training the model until it again converged. The resulting GP model provides and spatial and temporal estimate of the residuals of the groundwater model.

Combining the physical model and spatial model produces a model that approximates the physical flow of groundwater through the project area but also produces the best linear unbiased estimator of the well data. Figure 5.1 shows the estimated mean groundwater depth along an approximately 14 km-long section of the study area. Figure 5.2a shows the resulting estimate of the mean groundwater depth in January 2017 (the time the Lidar data was collected) along cross-section A-A'. Figure 5.2b shows the temporal variation of the groundwater depth near well 48685.

[65] U.S. Geological Survey (2019). National Hydrography Dataset (USGS National Hydrography Dataset Best Resolution) (NHD). https://apps.nationalmap.gov/downloader/. Accessed January 1, 2021.
[66] Matthews et al. (2017). See note 62.

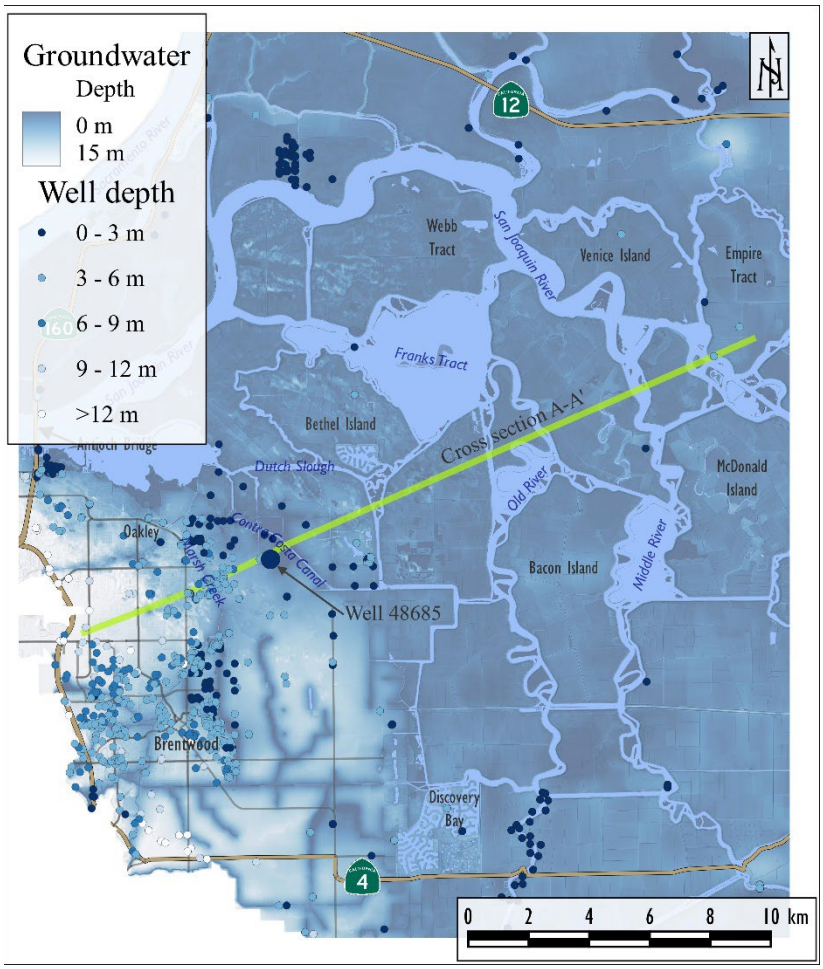

Figure 5.1. Mean estimated groundwater depth based on GP model regression from well observations

These figures demonstrate the importance of temporal fluctuations in groundwater conditions, which may influence soil liquefaction analyses. The combined physical and GP model indicates that the mean groundwater elevation at well 48685 has increased from an elevation of approximately -0.5 m (NAVD88) in 2010 to 2.1 m in 2020. The groundwater elevation of 12 other frequently monitored wells within a 5 km radius of well 48685 has also increased, on average, from an approximate elevation of -0.6 m to 2.7 m over the same period. Borings near well 48685 indicate that layers of loose to medium dense, fine silty sand are present above elevation 0.0 m. These soils are susceptible to liquefaction when saturated, and as the mean groundwater elevation has risen, the probability of soil saturation and liquefaction susceptibility has also increased.

Plate A-1 shows the estimated mean groundwater depth in January 2017 for the entire study area. The plate also shows measured groundwater depths at the various groundwater monitoring and observation wells.

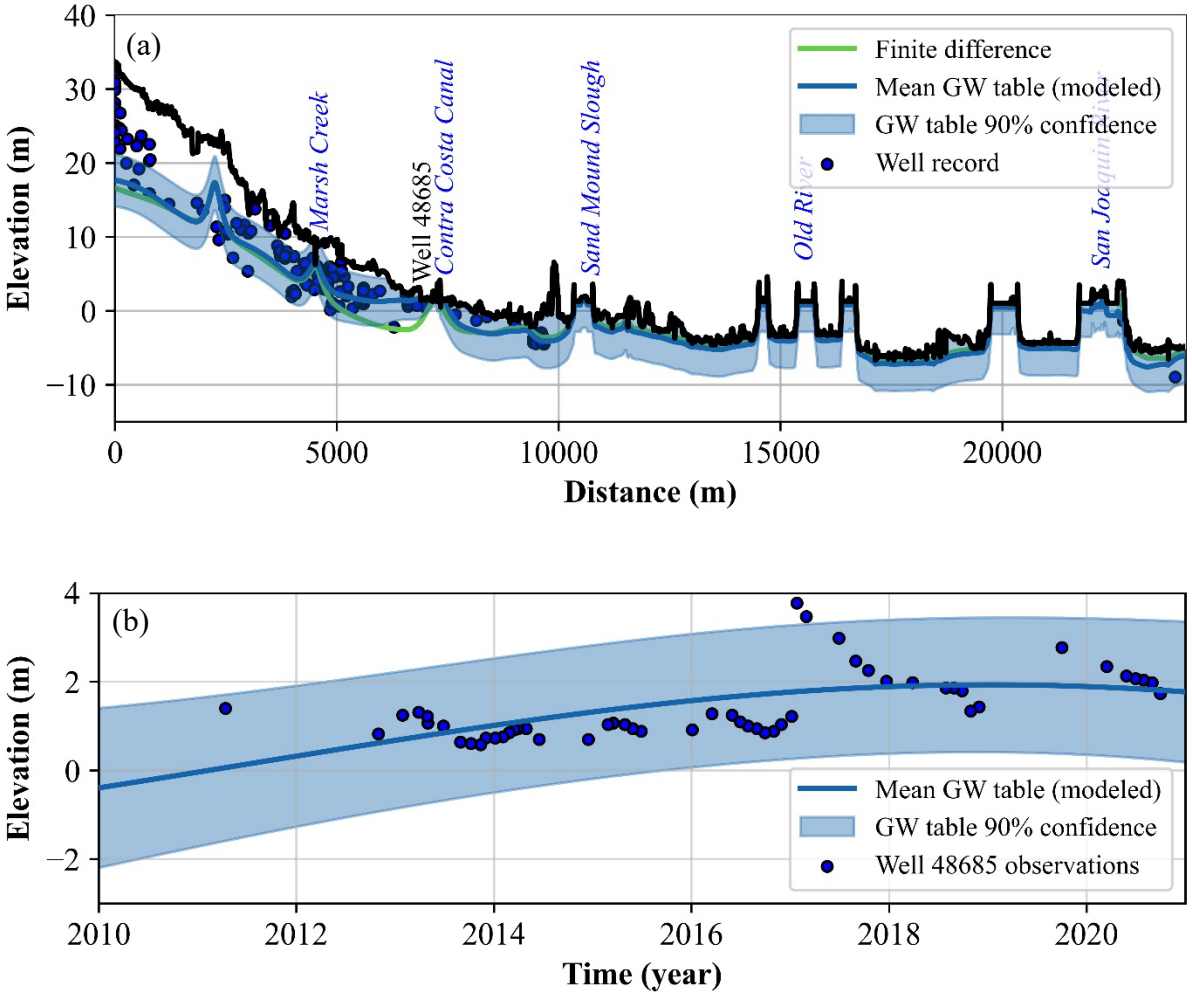

Figure 5.2. Spatial and temporal probability of saturation: (a) along section A-A' during January 2017 and (b) at well 48685. Map locations are shown in Figure 5.1.

5.3. Validation

We set aside groundwater data from 20 randomly selected wells in a blind holdout dataset that was not used to fit GP models. The holdout data is geographically distributed throughout the study area such that static groundwater elevations range from -3.3 to 31.6 m. Liquefaction is most likely in areas of shallow groundwater, and 15 of the wells have a static groundwater depth less than 6 m deep. The combined physical and GP models correctly classify groundwater as shallow or deep (less or greater than 6 m) at 85% of the locations. Two of the misclassifications occur at locations where the static groundwater depth is 5.9 and 6.3 m deep, which are very close to the 6 m classification threshold. These results demonstrate that the model correctly predicts the locations of shallow groundwater in a blind holdout dataset with at least 85% confidence.

6. Geologic deposit modeling

6.1. Gaussian process classifiers

To address the unknown thickness of each geologic deposit, we first classify the geology observations at each sampling location (e.g., the geologic interpretation of a split-spoon sample) using a one-of-*m* class encoding scheme[67], where *m* is the number of geologic deposits in the area. A geologic deposit classification model is then constructed from *m* latent GPs which each provide mean values that may be transformed to estimate the probability that a sample belongs to a specific class via classification operators.

In our geologic classification dataset, each sample is weighted based on its representative measurement interval, with SPT measurements weighted based on a 0.45 m penetration interval and CPT measurements weighted based on a 0.05 m penetration interval. We use a robust-max classification link function (equation 4.3.7) to transform the mean value of the *m* latent GPs into a probability of encountering each geologic deposit. Murphy[68] and Matthews[69] provide additional details regarding GP classifiers are their implementation into GPFlow. We fit the hyperparameters of the multiclassification GP model based on the one-of-*m* encoding using GPFlow. Table 6.1 provides the trained hyperparameters of the geologic deposit model.

Table 6.1: Geologic model hyperparameters

Hyperparameter	Value
Number of latent GPs, *m*	6
Misclassification rate, ε	0.151
Horizontal length scale, *s*	683 m
Vertical anisotropy factor, s_v	201

Knowledge of the general geologic structure of the area, observations from historical sources such as water wells and pile driving records, recent projects in the area, and other considerations that are often referred to as "engineering judgment" may be incorporated into the GP classification models using Bayesian updating. For example, local experts estimate that the likelihood of encountering Pleistocene soils (Qp) increases significantly below a depth of about 15 m. These judgment-based prior probabilities may be used in combination with the data-trained GP classification model, such that:

$$P[geo_i|c_i] = \frac{P[c_i|geo_i]P[geo_i]}{\sum_k P[c_k]P[geo_k]} \tag{6.1.1}$$

where $P[geo_i|c_i]$ is the posterior probability that a new sample belongs to geologic deposit geo_i, c_i is the GP classifier for geo_i, $P[c_i|geo_i]$ is the robust-max classification for c_i, and $P[geo_i]$ is

[67] Williams, C.K.I. and Barber, D. (1998). "Bayesian Classification with Gaussian Processes." *IEEE Transactions on Pattern Analyses and Machine Intelligence*. 20(12).
[68] Murphy, K.P (2012). *Machine Learning: A probabilistic perspective*. The MIT Press.
[69] Matthews et al. (2017). See note 62.

the assumed prior probability that the sample belongs to geo_i. The posterior geologic classification at any new location is calculated as $\text{argmax}_i\ P[geo_i|c_i]$.

Prior knowledge of geologic conditions in the area includes the available geologic maps and the general intuition that older soils are more likely to be encountered with depth. To estimate $P[geo_i]$ in equation (6.1.2), we created a second GP model fit to pseudo data that represents our judgment-based assumptions. We generated the pseudo data by converting the geologic maps to a 10 m grid. We then added undifferentiated Pleistocene soil (Qp) pseudo-samples at depths ranging from 15 to 45 m deep over 10% of the project area to account for the likely increased probability of Pleistocene soils at depth. We fit the second, judgment-based GP model using the same procedure as the subsurface data-derived model for $P[c_i|geo_i]$.

The data-supported GP converges to the borehole observations with a misclassification rate ε, but then the uncertainty in the geologic classification increases with distance from the borings. The judgment-based GP model approximates the geologic maps at the ground surface, but then the uncertainty increases with depth. Eventually, the judgment-based model predicts Pleistocene soils at depths greater than 15 m. Combining the two models using equation (6.1.1) results in a model that approximates the mapped geology at the ground surface but also converges towards borehole observation data.

To illustrate the computation of the posterior probability and predicted classification, Table 6.2 provides an example computation of the probability of a sample belonging to the dune sand (Qd) geologic deposit at the location of boring cgl-2002-b9 near the Contra Costa Canal. Figure 6.1 shows the location of cgl-2002-b9 within the study area. The ground surface in the vicinity of boring cgl-2002-b9 is mapped as Holocene alluvium (Qha), but the area is interlaced with dune sand deposits. The depth of either the alluvium or dune deposits is not explicitly described in the geology maps, but the boring log indicates mixtures of silty clay, clayey silt, sand sandy silt of the Qha deposit extend from the ground surface to a depth of approximately 1.5 m. Silty sand and sand with silt members of the dune (Qd) deposit lie below the Qha soils and extend to the maximum depth explored of 6 m. The prior, judgment-based probability in Table 6.2 illustrates the general assumptions about the area: dune soils may be present at shallow depths, but the intermixing of alluvium and dune deposits lead to considerable uncertainty at shallow depths. The data-derived GP model then predicts that dune soils are present at sample locations below 1.5 m deep with probabilities approaching $1 - \varepsilon$, matching the boring log observations.

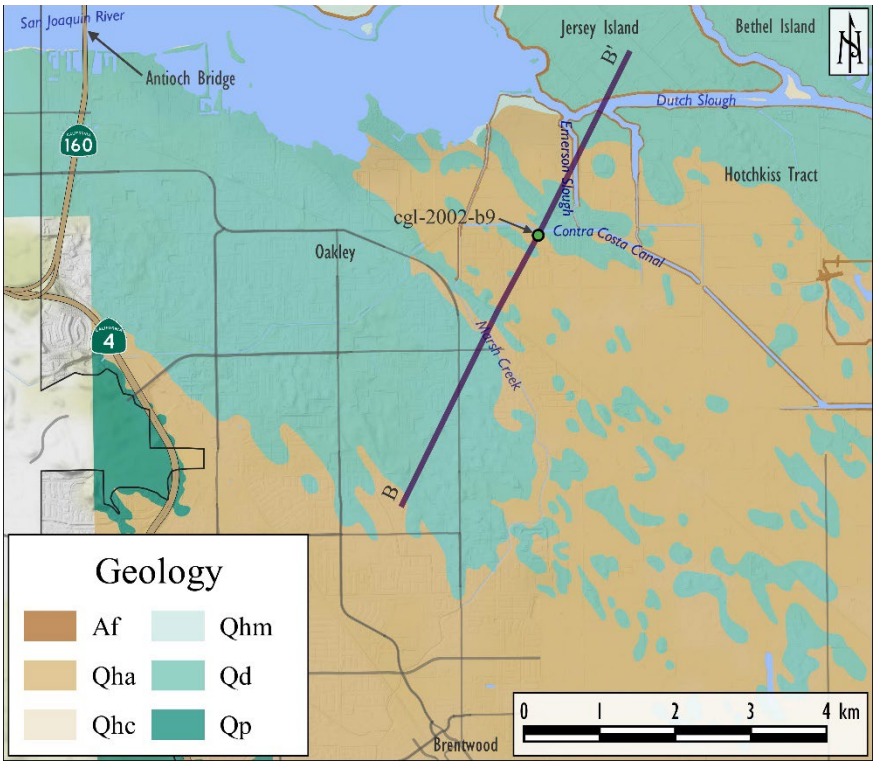

Figure 6.1 – Location of Cross-section B-B'

Table 6.2: Example calculation of the probability of Qd membership at cgl-2002-b9

Sample depth, m	Prior, $P[Qd]$	GP model, $P[c_{Qd}\|Qd]$	Marginal likelihood, $\sum_k P[c_k]P[geo_k]$	Posterior, $P[Qd\|c_{Qd}]$	Predicted class	Actual class
0.9	0.47	0.16	0.36	0.21	Qha	Qha
1.8	0.32	0.84	0.30	0.91	Qd	Qd
3.4	0.46	0.85	0.41	0.96	Qd	Qd
4.9	0.07	0.85	0.08	0.67	Qd	Qd

At a location approximately 1,000 m northwest of cgl-2002-b9 near Emerson Slough, boring data is absent. The area is mapped as a dune soil deposit, but the geologic maps also show that alluvial deposits may be interlaced with dune deposits in the area. No borehole data is nearby to support the GP model, so the judgment-based prior probabilities have a greater influence on the posterior probabilities. Table 6.3 shows the same computation as Table 6.3 but at the Emerson Slough location, illustrating the influence of the prior probability at locations without sample data.

Table 6.3: Example calculation of the probability of Qd membership near Emerson Slough

Sample depth, m	Prior, $P[Qd]$	GP model, $P[c_{Qd}\|Qd]$	Marginal likelihood, $\sum_k P[c_k]P[geo_k$	Posterior, $P[Qd\|c_{Qd}]$	Predicted class	Actual class
0.9	0.84	0.07	0.09	0.64	Qd	Qd[1]
1.8	0.86	0.08	0.09	0.76	Qd	-
3.4	0.68	0.17	0.18	0.66	Qd	-
4.9	0.85	0.38	0.34	0.93	Qd	-

[1] Based on the geologic map

Figure 6.1 shows a plan view of the prior ground surface geologic assumptions with the location of cross-section B-B', which intersects both cgl-2002-b9 and the Emerson Slough. The ground surface along cross-section B-B' is primarily mapped dune soils, except for a segment approximately 3,000 m long near the Contra Costa Canal where interfingered zones of dune and alluvial soils are mapped. As illustrated in Table 6.2, the borehole data in the vicinity of cross-section B-B' suggest that dune soils may be present at shallow depths even at locations where alluvium mantles the ground surface. Figures 6.2a through 6.2c show the prior, GP, and posterior probabilities of encountering dune soils along cross-section B-B'. The closed circle data points in Figures 6.2a through 6.2c correspond to the geology classifications from split spoon samples and CPT data. The combination of the prior assumptions with the GP model indicates that thick deposits of dune soils are likely along the first 2,500 m of the cross-section, but the interfingered dune and alluvium deposits lead to considerable uncertainty in the 3,000 m-long segment near the Contra Costa Canal. Northeast of the Emerson Slough, the posterior probabilities indicate that dune deposits likely mantle the ground surface and extend to depths greater than 10 m.

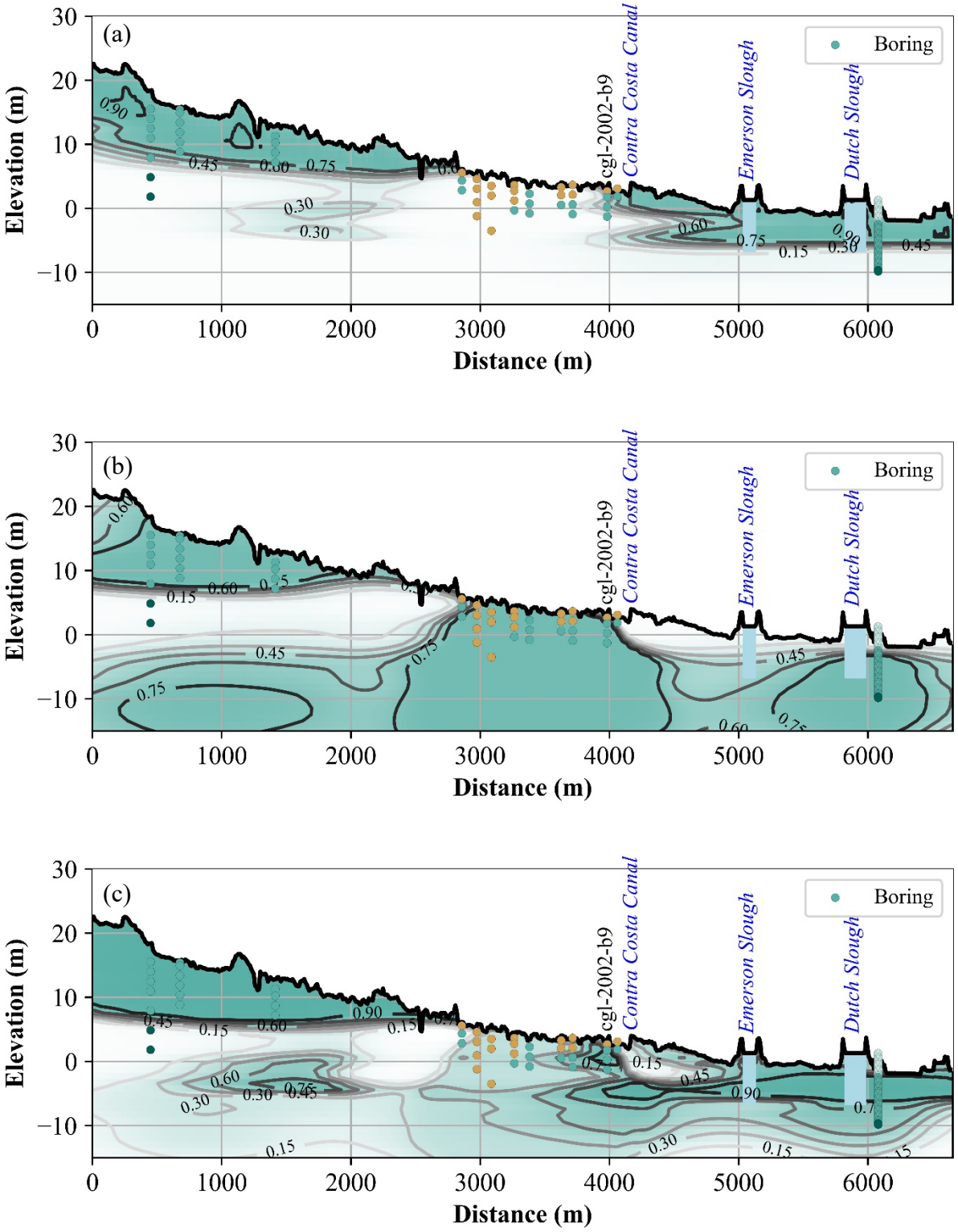

Figure 6.2 – Cross-section B-B' with (a) prior distribution of Qd, (b) GP estimate of Qd, and (c) posterior distribution of Qd. Filled circles represent sample observations (see Figure 6.3 for color legend)

We repeated the Bayesian updating calculations for all 6 geologic units. Figure 6.3 shows the most likely classification of the geologic deposit along cross-section B-B'.

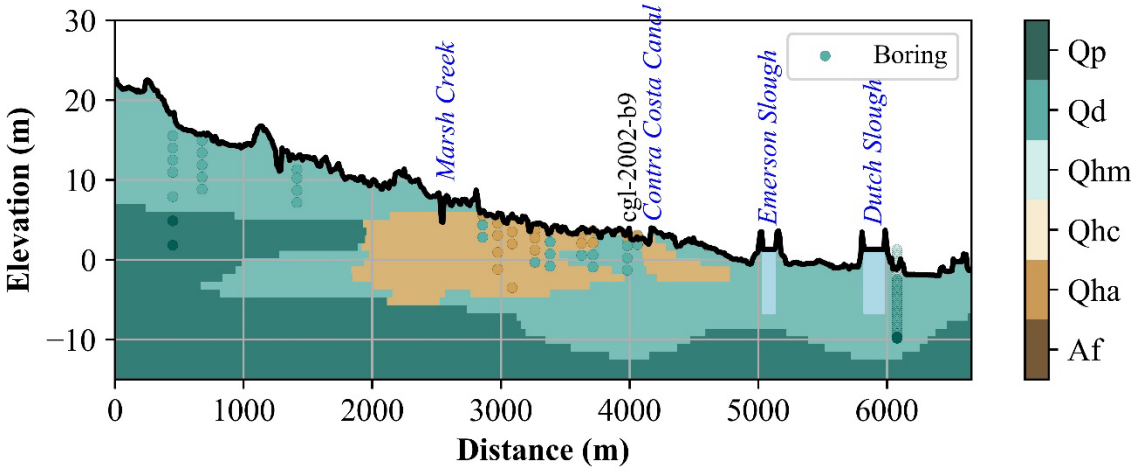

Figure 6.3 – Cross-section B-B' with most likely geologic deposit classification. Filled circles represent sample observations

6.2. Validation

We set aside geologic deposit data from 20 borings with a total of 159 sample classifications as a blind holdout dataset that was not incorporated into the model during the development and GP hyperparameter fitting stages. The most likely deposit of the posterior geology model correctly classifies about 75% of the samples in the blind holdout dataset. A random process would result in about 17% correct classification. Simply using the mapped surface geology to classify samples at all depths would result in about 44% correct classification, demonstrating the need for 3D representation of the subsurface conditions.

7. Liquefaction susceptibility and triggering modeling

To evaluate the probability of liquefaction triggering over a regional scale, geospatial estimators are needed for the random variables to assess the probability of liquefaction susceptibility ($P[sand]$) and the probability of the cyclic stress ratio being greater than the cyclic resistance ratio ($P[CSR > CRR|sand]$). The expansion of the site-specific liquefaction triggering equations (i.e., Equations 4.1.1 through 4.1.4) allows for estimates of the CRR based on the GP estimator of penetration resistance. Section 3.5 describes geologic deposit-based statics for these properties. Equation (4.2.2) also implies that the soil behavior classifiers and penetration resistance estimates may be calculated as independent random variables for each geologic deposit via the expansion of the total probability theorem.

7.1. Gaussian process classifier for soil behavior classification

We separate the soil behavior classifications for each geologic deposit into 6 independent datasets and fit GP classifier models using GPFlow[70]. We link the continuous values of the latent GP models to binary classifiers via an inverse standard normal distribution (probit) function. The transformation allows for regression using standard gradient methods. We utilize the stochastic variational model in GPFlow and sample the training dataset according to the weights assigned to SPT and CPT sample intervals described previously. We then evaluate the anisotropy of soil behavior classifications by fitting an independent length scale hyperparameter on the vertical dimension of the GP classifiers for each geologic deposit. Table 7.1 shows the resulting hyperparameters of the GP classification model for sand-like soil behavior classification. The sill in Table 7.1 is described in terms of the square root of variance for comparison to the standard deviation values listed in the deposit statistics of Table 3.1.

Table 7.1: GP hyperparameters for latent liquefaction susceptibility classifiers

Soil deposit	Mean	Sill, $\sqrt{{\sigma_y}^2 + {\tau_y}^2}$	Length scale, s	Anisotropy factor, s_v
Af	-1.649	1.186	2,410 m	4,710
Qha	-0.613	0.501	2,180 m	703
Qhc	-1.335	0.988	1,440 m	942
Qhm	-1.679	0.621	505 m	288
Qd	1.996	0.739	316 m	181
Qp	-0.791	0.508	671 m	119

Since independent soil classification GPs are developed for each geologic deposit, the uncertainty in geologic deposit also contributes to the uncertainty in soil behavior classification. Table 7.2 shows the probability of soil liquefaction susceptibility for Holocene alluvium and dune deposits at boring cgl-2002-b9, with the most likely deposit highlighted. Continuing the example provided in the previous section, the ground surface in the vicinity of cgl-2002-b9 is primarily composed of soils associated with the Holocene alluvium deposit, which include mixtures of silty clay, clayey silt, sand sandy silt. Boring cgl-2002-b9 indicates clay-like soils associated with the Holocene alluvium deposit mantle the ground surface. However, boring cgl-2002-b8 was drilled approximately 250 m to the west and indicates sand-like soils associated with the Holocene alluvium deposit mantle the ground surface. The mixture of sand-like and clay-like alluvial soils within the length scale of 2,180 m near cgl-2002-b9 leads to considerable uncertainty in the GP soil behavior classifier for Holocene alluvium. As a result, the GP classifiers estimate the probability of encountering sand-like soils at a depth of 0.9 m in the Holocene alluvium is approximately 60%. Below a depth of 1.8 m, soils associated with the dune deposit are more likely and the GP classifiers correctly classify the presence of sand-like soils of the dune deposit with probabilities ranging from 98 to 100%.

[70] Matthews et al. (2017). See note 62.

Table 7.2: Example calculation of the probability of sand-like soil behavior near cgl-2002-b9. The most likely geologic deposit is highlighted.

Sample depth, m	$P[Qha]$	$P[sand\|Qha]$	$P[Qd]$	$P[sand\|Qd]$	Borehole cgl-2002-b9 sample classification
0.9	0.78	0.60	0.21	1.00	Qha, clay-like with lenses of sand-like soils nearby
1.8	0.08	0.59	0.91	1.00	Qd, sand-like
3.4	0.03	0.56	0.96	0.99	Qd, sand-like
4.9	0.31	0.51	0.67	0.98	Qd, sand-like

7.2. Gaussian process regression for penetration resistance

Each geologic deposit is associated with an independent set of penetration resistance samples. To maintain independence between liquefaction susceptibility and triggering assessments, we only use data from sand-like samples to develop the GP estimators of penetration resistance. We first transform the penetration test data to a log-normal distribution and then standardize the data by subtracting the transformed mean and dividing it by the transformed standard deviation. We then fit the hyperparameters of the GP regression models using the stochastic variation process in GPFlow described previously. Table 7.3 lists the resulting optimized hyperparameters of the GP models for penetration resistance. The nugget and sill are listed in terms of the square root of variance for comparison to the standard deviation values listed in Table 3.1.

Table 7.3: GP hyperparameters for penetration resistance of susceptible soils

Soil deposit	Nugget, τ_y	Sill, $\sqrt{{\sigma_y}^2 + {\tau_y}^2}$	Length scale, s	Anisotropy factor, s_v
Af	0.268	0.753	181 m	248
Qha	0.248	0.621	655 m	181
Qhc	0.307	0.566	322 m	57
Qhm	0.256	0.710	809 m	552
Qd	0.328	0.665	338 m	93
Qp	0.269	0.554	1,100 m	218

The length scale and vertical anisotropy factors in Table 7.3 indicate the vertical correlation length ranges from 0.7 m in the Af deposit to 5.0 m in the Qp deposit. These values generally correspond with the previously reported values. For example, Greenfield and Grant[71] report

[71] Greenfield and Grant (2020). See note 7.

vertical correlation lengths (*s*) ranging from about 0.8 to 2.2 m for standard penetration test results in artificial fill and alluvium units in Portland, Oregon. Phoon and Kulhway[72] report vertical fluctuation scales (approximately 1.64 *s* for 90% confidence) of 2–6 m for uncorrected SPT penetration resistance in sandy soils from a large database from many different locations. Figure 7.2 shows the spatial variability of the GP-estimated penetration resistance for sand-like dune soils along cross-section B-B' at a depth of 2 m. The figure also shows the sample measurements from sand-like dune soils within the length scale of the optimized GP soil behavior classifier. The size of each dot in Figure 7.2 represents the spatial proximity of the data to the cross-section, with larger points corresponding to closer observations. The median GP estimates reflect the general trends of penetration resistance decreasing from the greatest values at the southern end of the cross-section to the lowest values at the northern end. The figure also demonstrates that the penetration resistance of geologic deposits is not spatially uniform and that the spatial interpolation provides a better estimate of the penetration resistance than the deposit-based average.

The optimized maximum likelihood nugget values in Table 7.3 also indicate that the spatially independent nugget of the log of penetration resistance ranges from approximately 0.25 to 0.33 within the Qha and Qd deposits. These values are significantly greater than the assumed spatially independent standard deviation implied by the site-specific simplified liquefaction triggering methods[73], which range from approximately 0.15 and 0.20. As a result, the optimized maximum likelihood estimates of penetration resistance are much more uncertain than assumed by the site-specific methods. The effect of the relatively large spatially-independent uncertainty is illustrated in Figure 7.2, which shows the median and 90% confidence interval range of $(N_1)_{60cs}$ of the dune soil deposits along cross-section B-B'. At the locations of relatively dense sampling, the standard deviation of the GP estimator decreases to about 0.41. At locations with relatively infrequent sampling, the standard deviation of the GP estimator increases to values of up to 0.60. Approximately 96% of the data lie within the 90% confidence intervals, and the optimized model neither interpolates the data points nor does it result in an overly wide confidence interval.

[72] Phoon K-K and Kulhway F.H. (1999). Characterization of geotechnical variability. *Can Geotech J* 36(4):612–24.

[73] Boulanger and Idriss (2012), see note 39; Boulanger and Idriss (2016), see note 37.

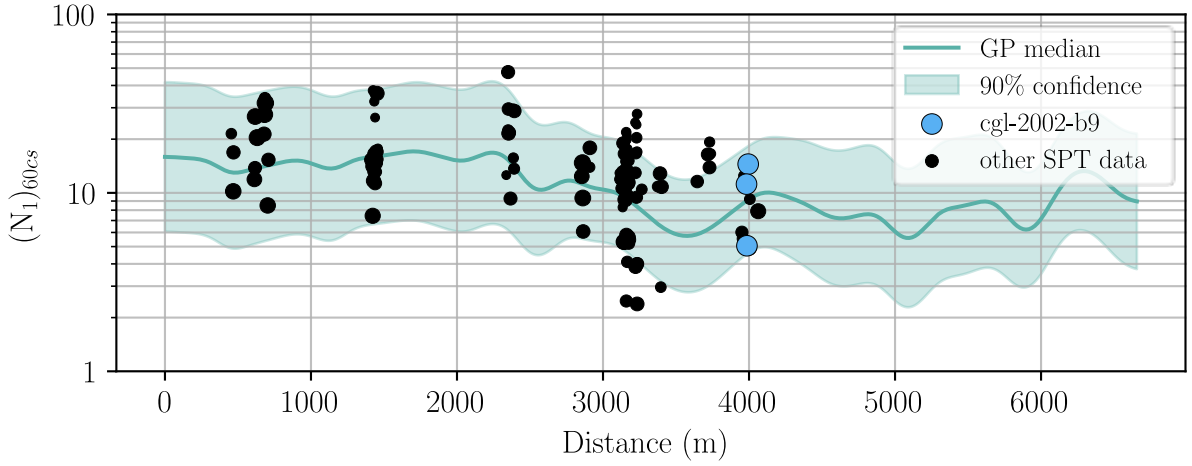

Figure 7.2 –GP estimates of penetration resistance in dune soils at a depth of 2 m along cross-section B-B'. The size of each dot represents the spatial proximity of the data to the cross-section, with larger points corresponding to closer observations.

Continuing the previous example at cgl-2002-b9, the GP model estimates a 90% confidence interval of $(N_1)_{60cs}$ values ranging from 5 to 18 blows/ft with a median $(N_1)_{60cs}$ of 9 blows/ft. The measured overburden and fines-corrected $(N_1)_{60cs}$ values of the dune sand samples at cgl-2002-b9 range from 5 to 14 blows/ft with a median $(N_1)_{60cs}$ of 9 blows/ft. These values correspond to the GP model over the vertical length scale of the model.

7.3. Validation

Using the same blind holdout set as described previously with 159 samples from 20 borings, we calculated the probability of liquefaction susceptibility and penetration resistance based on the independent GP models for each geologic deposit. Given the appropriate geologic deposit classification (i.e., the conditional probability of equation (4.2.2)), we calculate the probability of each sample exhibiting sand-like soil behavior. We then classify the samples as clay-like or sand-like based on the most likely soil behavior classification (greater or less than 50% probability). The resulting susceptibility models correctly classify 81% of the samples in the blind holdout dataset.

We repeat the analysis for penetration resistance to identify samples that are medium dense or looser with median $(N_1)_{60cs}$ values less than 15 blows/ft. Only liquefaction susceptible samples were used in the validation analysis of penetration resistance, resulting in a smaller holdout dataset of 34 samples. The penetration resistance models correctly classify 94% of the samples in the blind holdout dataset.

8. Ground damage

8.1. Spatial analysis of liquefaction

The independent GP estimators for groundwater depth, geology classification, soil behavior classification, and penetration resistance provide the needed geospatial estimators to compute the probability of liquefaction using equation (4.2.2) at any location within the study area. To disaggregate the contribution of the liquefaction probability by geologic deposit for demonstration purposes, we regroup the terms in equations (4.2.2) through (4.2.4) as:

$$P[liq] = \sum_{geo} P[sat]P[sand, geo]P[CSR > CRR|sand, geo]\,P[geo] \qquad (7.2.1)$$

The probabilities of soil saturation, geologic deposit classification, and soil behavior classification are readily calculated from the GP regression or classification models described previously. We use the GP-estimated median and standard deviation of $(N_1)_{60cs}$ penetration resistance to calculate the *CRR* using equations (4.1.2) and (4.1.4). We calculate the *CSR* at arbitrary locations using equation (4.1.3) for scenario events. Table 8.1 lists the calculation of the probability of liquefaction triggering at cgl-2002-b9 for an M7.1 Hayward Fault scenario with a *PGA* of 0.22 g. Table 8.1 also shows the deterministic site-specific liquefaction triggering estimates[74] with an assumed groundwater depth of 0.9 m.

Table 8.1: Calculation of probability of the liquefaction at cgl-2002-b9 for an M7.1 Hayward Fault scenario earthquake with *PGA* of 0.22 g.

Sample depth, m	$P[sat]$	$P[sand\|Qd]$	$P[CSR > CRR\|sand, Qd]$	$P[Qd]$	$P[sat] \cdot P[sand\|Qd] \cdot P[CSR > CRR\|sand, geo] \cdot P[Qd]$	Total probability, $P[liq]$	Site-specific deterministic
0.9	0.51	1.00	0.44	0.21	0.05	0.20	Not susceptible
1.8	0.68	1.00	0.56	0.91	0.40	0.43	Liquefaction
3.4	0.89	0.99	0.62	0.96	0.62	0.64	Liquefaction
4.9	0.98	0.98	0.52	0.67	0.42	0.58	Liquefaction

The consequence of uncertainty in the groundwater depth, geologic deposit, soil behavior classification, and penetration resistance leads to probabilities of liquefaction in the vicinity of cgl-2002-b9 that range from 20% to 64%. The regional model indicates the sample least likely to

[74] Boulanger and Idriss (2012). See note 39.

liquefy is at a depth of 0.9 m, where the probability of saturation is the lowest and the probability of encountering clay-like alluvial soil is the greatest. The samples below a depth of 1.8 m are estimated to be members of the Qd soil deposit, with cumulative probabilities of liquefaction ($\sum_{geo} P[liq|geo]\, P[geo]$) as great as 64%. The sample most likely to liquefy is at a depth of 3.4 m, where the probability of encountering saturated, sand-like, loose to medium dense dune soils is the greatest.

Boring cgl-2002-b9 indicates that saturated, sand-like samples with blow counts ranging from 5 to 14 blows/ft were encountered between depths of 1.8 and 6 m. The median penetration resistance of the liquefaction-susceptible samples is 9 blows/ft. Based on the median penetration resistance, the cyclic stresses from the Hayward Fault scenario event are greater than the cyclic resistance, also indicating that liquefaction is likely.

8.2. Ground damage classification

Green and others[75] describe a classification system for liquefaction severity based on the fraction of an area that exhibits liquefaction ground damage from past case histories. Random realizations of Gaussian fields indicate that the fraction of the area damage may be approximated by the probability of liquefaction ground damage if the length scale hyperparameter (*s*) is very small relative to the area of interest. For this study, we have assumed that the length scales are sufficiently small that the fraction of the damaged area may be approximated by the probability of liquefaction ground damage. Table 8.2 (modified from Green and others) provides a link between the spatial extent of liquefaction manifestation and various liquefaction severity classifications.

Table 8.2. Liquefaction severity classification

Classification	Probability of liquefaction manifestation
No liquefaction	< 1%
Minor liquefaction	1 to 5%
Moderate liquefaction	5 to 40%
Severe liquefaction	40 to 100%

8.3. Liquefaction ground damage

Assuming each depth increment represents the top of the liquefiable layer (H_1), we calculate the value of H_2 necessary to produce ground damage using equations (4.2.3) and (4.2.4):

$$P[L] = \sum_{geo} P[liq_{H_1}] P[liq_{H_1+H_2}|liq_{H_1}] \quad (7.2.2)$$

[75] Green, R.A, Maurer, B.W. and Sjoerd van Ballegooy (2018). The Influence of the Non-liquified Crust on the Severity of Surficial Liquefaction Manifestations: Case History from the 2016 Valentine's Day Earthquake in New Zealand. *Geotech. Earthquake Eng. & Soil Dynamics*, V GSP 290.

where $P[L]$ is the probability of liquefaction ground damage, defined as the joint probability of liquefaction at depths H_1 and $H_1 + H_2$. Equation (7.2.2), which is identical to equation (4.23.), requires the computation of the conditional probabilities $P\left[sand_{H_1+H_2}|sand_{H_1}\right]$ and $P\left[CSR > CRR_{H_1+H_2}|CSR > CRR_{H_1}\right]$. To calculate these conditional probabilities, we transform the values of $P\left[sand_{H_1}\right], P\left[sand_{H_1+H_2}\right], P\left[CSR > CRR_{H_1}\right]$, and $P\left[CSR > CRR_{H_1+H_2}\right]$ using equations (4.2.5) through (4.2.7). We then estimate the correlation coefficients between H_1 and $H_1 + H_2$ using the Gaussian radial basis function (equation 4.2.8) and the length scale hyperparameters listed in Tables 7.1 and 7.3.

We iterate over all depth increments and define the probability of liquefaction ground damage at each location by the maximum probability from all depth increments. Table 8.3 lists the pseudocode to estimate the probability of liquefaction ground damage for a given *PGA*, earthquake magnitude, and location.

Table 8.3: Pseudocode algorithm for liquefaction ground damage for given *PGA*, M, and location

For z in depth:
  Assume $H_1 = z$
  For *geo* in geologic deposits:
    $P\left[liq_{H_1}|geo\right] = P[sat]P\left[sand_{H_1}, geo\right]P[CSR > CRR_{H_1}|sand_{H_1}, geo]$
    Calculate H_2 given H_1 and *PGA*
    $P\left[liq_{H_1+H_2}|liq_{H_1}, geo\right]$
      $= P\left[sand_{H_1+H_2}|sand_{H_1}, geo\right] P\left[CSR > CRR_{H_1+H_2}|CSR > CRR_{H_1}, sand_{H_1}, geo\right]$
  $P[L_{H_1}] = \sum_{geo} P[geo]P\left[liq_{H_1}|geo\right]P\left[liq_{H_1+H_2}|liq_{H_1}, geo\right]$
$P[L] = \max_{H_1=z} P[L_{H_1}]$

Table 8.4 lists an example computation of the probability of liquefaction ground damage and liquefaction severity classification at cgl-2002-b9. Based on the discretization used in the previous examples, the probability of liquefaction ground damage is 49% with the critical layer located between 3.4 and 7.6 m deep. This probability corresponds to a severe liquefaction classification in Table 8.2.

Site-specific liquefaction estimates using the subsurface data at cgl-2002-b9 may be used as a validation check. Geyin and Maurer[76] have developed fragility functions for the probability of liquefaction surface manifestation based on liquefaction potential index (*LPI*) and Ishihara-inspired liquefaction potential index (LPI_{Ish}). The ground motions associated with the Hayward

[76] Geyin, M. and Maurer, B.W. (2020). Fragility Functions for Liquefaction-Induced Ground Failure. *J. Geotech Geoenviron. Eng.* 146(12).

Fault scenario results in *LPI* and LPI_{Ish} values of 11.1 and 11.8, respectively. These values correspond to a probability of liquefaction manifestation greater than 99%.

Table 8.4: Example calculation of the probability of the liquefaction ground damage at cgl-2002-b9 for an M7.1 Hayward Fault scenario earthquake with *PGA* of 0.22 g.

Sample depth H_1, m	$P[liq_{H_1}]$	H_2	$P[liq_{H_1+H_2}\|liq_{H_1}]$	$P[L]$
0.9	0.20	0.8 m	1.00	0.20
1.8	0.43	1.6 m	0.97	0.42
3.4[1]	0.64	4.2 m	0.76	0.49
4.9	0.58	28.4 m	0.59	0.35

[1] Critical layer

We use our estimates of groundwater depth, geologic deposit, soil behavior classification, and penetration resistance to estimate the probability of liquefaction for an array of *PGA* values ranging from 0.02 g to 1.0 g with earthquake magnitudes ranging from 5.5 to 8.5. At each location, we calculate the probability of liquefaction using equation (4.2.2) for the array of *PGA* and M values at depths ranging from 0.5 m to 20 m deep. We then use the pseudocode in Table 8.2 to calculate the probability of ground damage associated with the given *PGA* and M values on a 3 m grid throughout the study area, such that the probability of ground damage may be interpolated for arbitrary earthquake events.

8.4. Levee foundation instability

Both the DLIS[77] and DRMS[78] studies evaluate the seismic vulnerability of levees due to liquefaction and peat foundation instability. The preceding analyses provide a comprehensive method to evaluate the liquefaction ground damage probability at levee locations. However, to understand the potential for ground damage within the Delta, both the instability due to liquefaction and peat foundation instability must be considered.

The DRMS studies include fragility functions based on the thickness of organic deposits, the strength of the foundation material, and the levee geometry. At locations where the levee is not subject to liquefiable soils and not underlain by peat, the deformation of the levee crown is estimated as:

[77] DLIS (2017). See note 2.
[78] DRMS (2008). See note 13.

$$\ln(\delta) = -9.69 + 0.794M + 3.04PGA + 1.69w \quad (8.3.1)$$

where δ is the levee crown deformation in inches and w is a binary indicator equal to 1 if the waterside slope of the levee is steeper than 1.5H:1V and is 0 otherwise. The value of δ is assumed to be log-normally distributed with a lognormal standard deviation of 0.63. For levees underlain by peat, the estimated deformation from DRMS is defined as:

$$\ln(\delta) = -7.86 + 1.19M + 7.81PGA + 0.0464t - 0.0115c - 0.128\phi + 0.962w \quad (8.3.2)$$

where t is the thickness of peat in ft, c is the cohesion strength of the peat in psf, and ϕ is the friction angle of the peat. For this study, we use the mean strength estimates reported in DRMS of 120 psf cohesion and 28° friction angle. The value of δ is assumed to be log-normally distributed with a lognormal standard deviation of 0.595.

We calculate the thickness of peat underlying the levees in the study area based on the probability of encountering Holocene Delta mud (Qhm) soils of various thicknesses below the levee. The probability of encountering Delta mud at the bottom of the levee was first estimated using the GP geology classifiers. We then calculate the joint probability of encountering Delta mud soils at depths of 1, 3, and 7 m below the levee foundation using the joint probability estimates for an assumed latent bivariant normal distribution described in equations (4.2.5) through (4.2.7). The probability of levee damage is then defined as:

$$[D] = \sum_h P[H_{Qhm} > h]\Phi\left(\frac{\ln\delta - \ln\delta_D}{\sigma}\right) \quad (8.3.3)$$

where $P[D]$ is the probability of levee damage, $P[H_{Qhm} > h]$ is the probability of encountering a peat layer greater than h m thick, δ_D is a threshold deformation for damage, and σ is the lognormal standard deviation defined in equations (8.3.1) and (8.3.2). For this study, we assume the threshold deformation for levee damage is 0.025 m.

9. Scenario earthquakes

We use the methodology described in the previous sections to evaluate the liquefaction hazard at damaged levee locations following the 1980 M5.9 Livermore earthquake. We have also selected an M_w 7.1 Hayward Fault rupture scenario originating near Oakland[79] and an M_w 7.3 Midland Fault Zone rupture[80] to estimate the extent of ground damage from possible future earthquakes. At the levee locations, we also evaluate the probability of damage due to peat instability based on the DRMS fragility functions. Each of these scenarios is validated against observed data or site-specific estimates of liquefaction.

[79] Detweiler and Wein (2018). See note 20.
[80] BSSC (2015). See note 21.

9.1. Historic 1980 Livermore earthquake

Finch[81] reports damage along an approximately 75 m-long section of the east levee of Bacon Island during the 1980 M5.9 Livermore earthquake. The USGS Shakemap for this event indicates the *PGA* on Bacon Island was approximately 0.12 g. Our model indicates that the relatively modest *PGA* values result in less than a 1% probability of liquefaction ground damage on Bacon Island. However, the GP geologic classifications indicate the levees surrounding Bacon Island are likely underlain by thick peat deposits, resulting in an approximately 6% probability of levee damage.

Random, spatially correlated realizations of groundwater depth, geologic deposit, soil behavior classification, and penetration resistance may be drawn from the GP model distributions. We generate multiple realizations to evaluate the approximate areas of ground damage for a Livermore earthquake scenario. Figure 9.1 shows 4 random realizations of the extent of levee damage on Bacon Island. All 4 realizations result in levee damage due to peat instability, with the extent of the damage along the east levee ranging from approximately 50 to 110 m. All four realizations also result in liquefaction on Fay Island, but not on Bacon Island. These random realizations suggest that the damage to the east levee on Bacon Island was most likely a result of peat instability, not liquefaction. The realizations also suggest that levee damage approximately 50 to 110 m long is an expected outcome of the event.

We also use the GP estimators for groundwater depth, geologic deposit, soil behavior classification, and penetration resistance to estimate the probability of liquefaction on a 3 m grid throughout the study area. The estimated *PGA* within the study area ranged from 0.08 to 0.19 g. Based on the liquefaction severity classifications in Table 8.2, Plate A-2 shows the estimated liquefaction severity classifications throughout the study area. At the levee locations, we also evaluate the probability of levee damage due to peat instability. We have assumed these probabilities are independent of the probability of liquefaction and have combined them in the probability of ground damage assessment.

The results of the study-wide scenario indicate that moderate ground damage due to peat foundation instability is likely along the levees protecting Bacon Island. Liquefaction was unlikely in the vicinity of Bacon Island, but minor to moderate liquefaction was likely near the rivers on the south side of the study area in areas mapped as Qha. Minor to moderate liquefaction was also likely near the Contra Costa Canal.

[81] Finch (1985). See note 19.

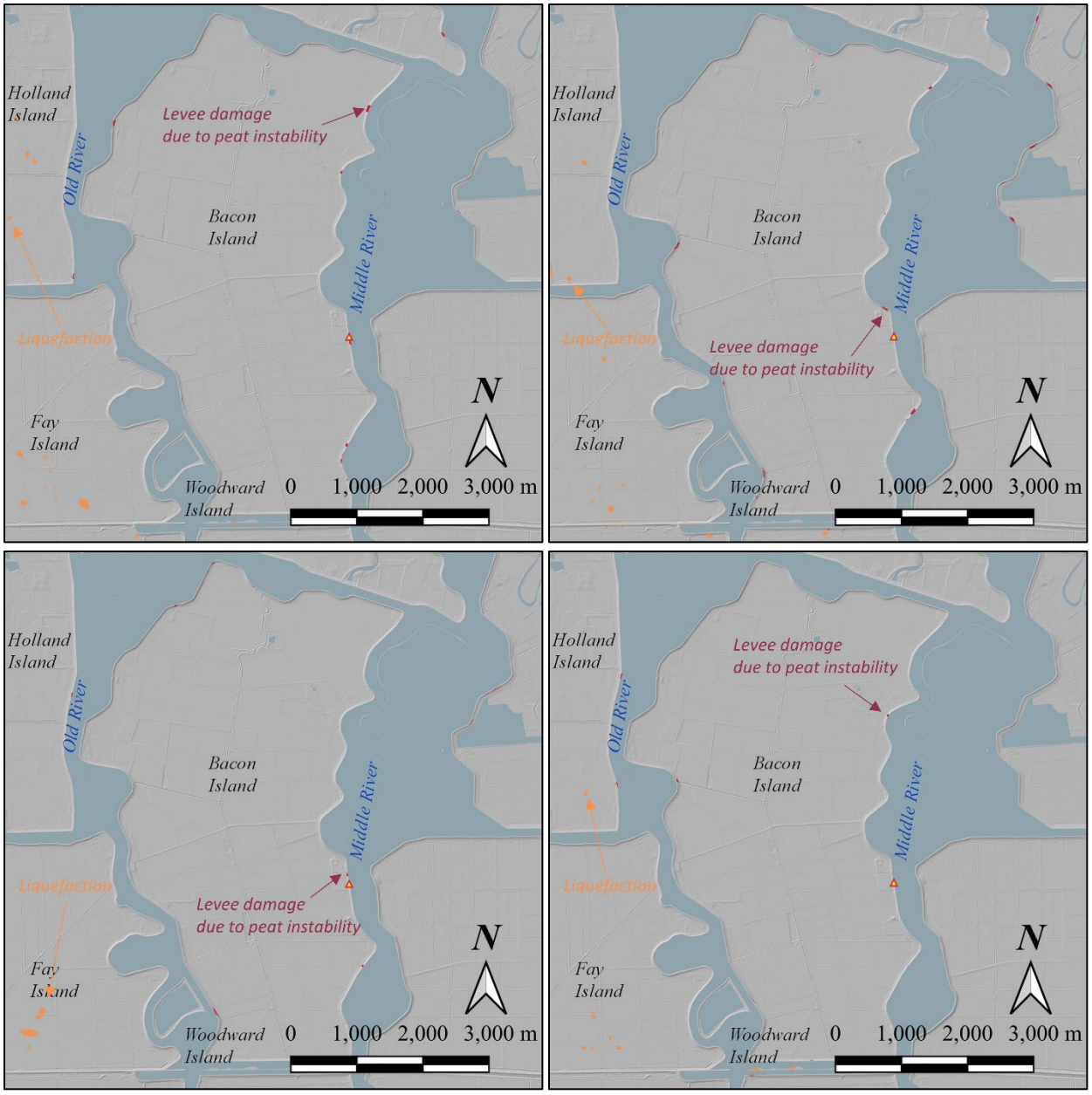

Figure 9.1 – Four random realizations of ground damage on Bacon Island. Red areas designate levee damage associated with peat instability. Orange areas designate liquefaction areas. The yellow triangle represents the approximate area of damage reported by Finch (1985).

Aside from the levee damage documented by Finch, we have identified no observations, either indicating the presence or absence of liquefaction, in the Delta following the Livermore earthquake. Since limited observational data is available for validation, we compare the regional scale liquefaction severity estimates to the fraction of borings and probes within each area designated as having no, minor, moderate, or severe liquefaction that would likely liquefy based on site-specific calculations. The liquefaction potential index (*LPI*) is also often used to evaluate the potential for liquefaction manifestation at the ground surface with site-specific data. Several

variants of *LPI* are available, including an *LPI* index that utilizes the Ishihara curves (LPI_{Ish}) as a limit state[82]. We have selected LPI_{Ish} for comparison to the regional scale probabilistic estimates since it utilizes the same liquefaction damage functions described by equations (4.1.6 and 4.1.7). Geyin and Maurer[83] have developed fragility curves of LPI_{Ish}, with values greater than 4.344 indicating liquefaction is likely. Table 9.1 shows the fraction of site-specific analyses that indicate liquefaction is likely within each of the designated liquation severity areas. Plate A-2 also shows the binary liquefaction classifications from the site-specific liquefaction estimates. The results indicate that the fraction of site-specific estimates aligns with the liquefaction severity categories.

Table 9.1. Liquefaction severity classification for the 1980 Livermore earthquake scenario

Classification	Probability of liquefaction manifestation	Fraction of site-specific estimates
No liquefaction	< 1%	0% (0/994)
Minor liquefaction	1 to 5%	1.0% (1/97)
Moderate liquefaction	5 to 40%	12.1% (7/58)
Severe liquefaction	40 to 100%	none

9.2. Historic 2014 Napa earthquake

The 2014 Napa earthquake is the most recent event within the San Francisco Bay Area that was strong enough to trigger liquefaction, although the Geotechnical Extreme Event Reconnaissance (GEER) Association[84] reports "a remarkable absence of liquefaction". Their reconnaissance identified only two liquefaction observations near Napa, over 80 km from the study area. The intensity of shaking within the Delta was weak, with estimated *PGA* values[85] ranging from 0.01 to 0.02 g. An analysis using the procedure described previously results in no liquefaction or levee damage within the project area.

9.3. Hayward Fault

We simulate ground damage from an M_w 7.1 Hayward Fault earthquake[86] to evaluate the potential for ground damage from a large earthquake within the San Francisco Bay area. The estimated *PGA* within the study area ranges from 0.14 to 0.25 g from this event and Plate A-3 shows the resulting extent of liquefaction ground damage. These analyses indicate that moderate liquefaction ground damage is likely throughout much of the areas mapped as dune sand where

[82] Maurer, B.W., Green, R.A., and Taylor, O.S. (2015). Moving towards an improved index for assessing liquefaction hazard: Lessons from historical data. *Soils and Foundations*, 55(4).
[83] Geyin and Maurer (2020). See note 76.
[84] Geotechnical Extreme Event Reconnaissance (GEER) Association (2014). Geotechnical Engineering Reconnaissance of the August 24, 2014 M6 South Napa Earthquake.
[85] U.S. Geological Survey. Earthquake Hazards Program: M 6.0 – South Napa: https://earthquake.usgs.gov/earthquakes/eventpage/nc72282711/executive.
[86] Detweiler and Wein (2018). See note 20.

shallow groundwater is present near the Contra Costa Canal, Dutch Slough, and San Joaquin River. Moderate liquefaction severity is also likely in areas of Holocene alluvium with shallow groundwater east of Brentwood. Isolated locations of severe liquefaction approximately 500 m across have also been identified. One of these locations is near boring cgl-2002-b9, which is an area where the groundwater is shallower and the soil deposits are looser than the deposit-scale averages may predict.

Just like the Livermore earthquake scenario, we compute LPI_{Ish} values at the boring and probe locations and classify the site-specific analyses as binary categories of no liquefaction or liquefaction. Table 9.2 shows the fraction of site-specific analyses within areas designated as having no, minor, moderate, and severe liquefaction as estimated based on the deposit-scale analyses. The table shows that the fraction of site-specific estimates aligns with each of the liquefaction severity categories. Plate A-3 also shows the deterministic site-specific analyses.

Table 9.2. Liquefaction severity classification for an M_w 7.1 Hayward Fault scenario

Classification	Probability of liquefaction manifestation	Fraction of site-specific estimates
No liquefaction	< 1%	0.7% (2/261)
Minor liquefaction	1 to 5%	1.5% (7/477)
Moderate liquefaction	5 to 40%	16.6% (65/392)
Severe liquefaction	40 to 100%	47.4% (9/19)

9.4. Great Valley Midland Fault Zone

Very strong to violent shaking is possible from an M_w 7.3 Great Valley Midland Fault Zone earthquake within the Delta. The estimated PGA[87] within the study area ranges from 0.30 to 0.71 g. Plate A-4 shows the resulting extent of liquefaction ground damage. These analyses indicate that severe liquefaction ground damage is likely throughout much of the areas mapped as dune sand or recent alluvium where shallow groundwater is also present. The area of severe liquefaction ground damage may extend 5 km or more inland from the San Joaquin River, especially in areas where canals may be elevating the local groundwater table. Moderate liquefaction severity is likely elsewhere, except for isolated locations east of Old River where a combination of lower shaking intensity and an increased likelihood of non-liquefiable peat soils results in minor liquefaction severity.

Just like the preceding scenarios, we compute LPI_{Ish} values at the boring and probe locations and classify the site-specific analyses into binary liquefaction categories. Table 9.3 lists the fraction of site-specific analyses within areas designated as having no, minor, moderate, and severe liquefaction. Plate A-4 also shows the binary classifications of the deterministic site-specific analyses.

[87] BSSC (2015). See note 21.

Table 9.3. Liquefaction severity classification an M_w 7.3 Great Valley Midland Fault Zone scenario

Classification	Probability of liquefaction manifestation	Fraction of site-specific estimates
No liquefaction	< 1%	0.0% (0/9)
Minor liquefaction	1 to 5%	26.9% (7/26)
Moderate liquefaction	5 to 40%	19.3% (130/673)
Severe liquefaction	40 to 100%	49.6% (219/441)

Table 9.3 indicates that the fraction of site-specific estimates aligns with each of the liquefaction severity estimates, except for the area designated as minor liquefaction. The minor liquefaction designation from the regional analysis underpredicts the liquefaction severity relative to the site-specific analyses. The 7 borings that would likely liquefy in the area mapped as minor liquefaction are within areas classified as peat deposits. However, the boring logs show that isolated layers of loose silty sand, which would likely liquefy during the very strong shaking, mantle the peat deposits. These borings were drilled outside of the levee fill areas, such that either the peat deposits contain significant amounts of sandy soils, or the geologic maps incompletely represent the soils in the area. A review of these borings indicates the uncertainty in the groundwater table is also a major component of the hazard. The assumption of mean groundwater elevation for the site-specific deterministic analyses results in layers of saturated silty sand that are thick enough to produce ground damage. But, lower-than-average groundwater elevations may result in the loose sandy layers becoming desaturated and not susceptible to liquefaction, reducing the potential for ground damage due to liquefaction. The effect of the misclassification of these 7 borings is likely spatially limited to the eastern side of the study area on Bacon Island, McDonald Island, and Staten Island. Nonetheless, the misclassifications in these areas demonstrate that further improvements in geologic mapping and groundwater modeling would help to better understand the liquefaction hazards at a regional level.

10. Conclusions

Engineers are increasingly using regional liquefaction analyses to evaluate liquefaction hazards for distributed infrastructure such as roadways, pipelines, levees, communication, and electrical distribution networks. Such analyses should consider the well-established procedures for site-specific liquefaction analyses while also accounting for the available geologic information and subsurface investigation data in the area. The methods developed for this study utilize probabilistic geospatial estimators of groundwater depth, geologic deposit classification, soil behavior classification, and penetration resistance to extend the concepts embedded in site-specific analyses to a regional scale.

Gaussian process (GP) models are ideal for this task since they produce unbiased fields of normally distributed random variables, such as soil behavior classification or penetration resistance, that converge towards the measured values at borehole and probe locations. Expanding on previous studies, we describe how GP models may be extended to large datasets and to classify

discrete data, like geologic deposit classification. The methods and results described here demonstrate that geospatial Gaussian process models can successfully unify site-specific and deposit-scale liquefaction hazard analyses by considering the uncertainty in groundwater depth, geologic deposit, soil behavior classification, and penetration resistance throughout an area of interest. Validation studies indicate that the Gaussian process models correctly classify 85% of the locations with shallow groundwater, 75% of the geologic deposit classifications, 81% of the soil behavior classifications, and 94% of loose sand-like samples in a blind holdout dataset of 20 borings and 159 samples. For comparison, simply relying on surface geology would correctly classify 44% of the samples in the holdout dataset. The probability of liquefaction associated with areas designed as having no, minor, moderate, or severe liquefaction also largely matches the fraction of site-specific analyses indicating that liquefaction is likely, further demonstrating that the probabilistic geospatial analyses successfully match site-specific observations.

Within the Sacramento-San Joaquin Delta, the Gaussian process models indicate that historic damage to levees due to distant earthquakes is likely the result of peat foundation instability. However, strong to very strong shaking associated with a Hayward Fault scenario may produce moderate liquefaction ground damage in the areas with shallow groundwater that are mapped as Holocene alluvium. Likewise, isolated locations with shallow groundwater where the late Pleistocene dune soils have been reworked with low penetration resistance near the Contra Costa canal may experience severe liquefaction during a Hayward Fault event. The combination of a local high groundwater elevation and looser-than-average deposits near the Contra Costa Canal could not have been identified using deposit scale average analyses, thus providing an example of where probabilistic geospatial interpolation analyses are needed to understand the hazard.

Acknowledgments

We would like to acknowledge Dr. Erik Frost, Dr. alex grant, Chris Hitchcock, and Dr. Lanka Ilankathran for providing subsurface data to support the analyses of this project. We would also like to thank the participants of our advisory panel, especially those who provided insightful comments which help guide the project. Finally, we would like to extend our gratitude to Dr. alex grant, whose collaboration and guidance made this project possible.

This material is based upon work supported by the U.S. Geological Survey under Grant No. G21AP10019-00.

Disclaimer

The views and conclusions contained in this document are those of the authors and should not be interpreted as representing the opinions or policies of the U.S. Geological Survey. Mention of trade names or commercial products does not constitute their endorsement by the U.S. Geological Survey.

Appendix A – Plates of groundwater depth and scenario ground damage estimates

Appendix A provides plates of the mean depth of groundwater and the estimated liquefaction severity classification for the historic 1980 M5.9 Livermore earthquake, an M7.1 Hayward Fault scenario, and an M7.3 Midland Fault Zone scenario earthquake. The USGS server is limited to files 10 MB in size and the plates exceed the allowable file size. If the plates are not attached at the end of this document, they may be accessed via DesignSafe at https://www.designsafe-ci.org/data/browser/public/designsafe.storage.published/PRJ-3406